Available online at www.sciencedirect.com
ScienceDirect
Journal of Computational Physics 227 (2008) 2154–2186
JOURNAL OF COMPUTATIONAL PHYSICS
www.elsevier.com/locate/jcp

A multigroup diffusion solver using pseudo transient continuation for a radiation-hydrodynamic code with patch-based AMR ☆

Aleksei I. Shestakov [a,*], Stella S.R. Offner [b,*]

[a] *Lawrence Livermore National Laboratory, P.O. Box 808, Livermore CA 94550, United States*
[b] *Physics Department, University of California, Berkeley CA 94720, United States*

Received 4 October 2006; received in revised form 10 September 2007; accepted 11 September 2007
Available online 6 October 2007

Abstract

We present a scheme to solve the nonlinear multigroup radiation diffusion (MGD) equations. The method is incorporated into a massively parallel, multidimensional, Eulerian radiation-hydrodynamic code with Adaptive Mesh Refinement (AMR). The patch-based AMR algorithm refines in both space and time creating a hierarchy of levels, coarsest to finest. The physics modules are time-advanced using operator splitting. On each level, separate "level-solve" packages advance the modules. Our multigroup level-solve adapts an implicit procedure which leads to a two-step iterative scheme that alternates between elliptic solves for each group with intra-cell group coupling. For robustness, we introduce pseudo transient continuation (Ψtc). We analyze the magnitude of the Ψtc parameter to ensure positivity of the resulting linear system, diagonal dominance and convergence of the two-step scheme. For AMR, a level defines a subdomain for refinement. For diffusive processes such as MGD, the refined level uses Dirichlet boundary data at the coarse–fine interface and the data is derived from the coarse level solution. After advancing on the fine level, an additional procedure, the sync-solve (SS), is required in order to enforce conservation. The MGD SS reduces to an elliptic solve on a combined grid for a system of G equations, where G is the number of groups. We adapt the "partial temperature" scheme for the SS; hence, we reuse the infrastructure developed for scalar equations. Results are presented. We consider a multigroup test problem with a known analytic solution. We demonstrate utility of Ψtc by running with increasingly larger timesteps. Lastly, we simulate the sudden release of energy Y inside an Al sphere ($r = 15$ cm) suspended in air at STP. For $Y = 11$ kT, we find that gray radiation diffusion and MGD produce similar results. However, if $Y = 1$ MT, the two packages yield different results. Our large Y simulation contradicts a long-standing theory and demonstrates the inadequacy of gray diffusion.
Published by Elsevier Inc.

Keywords: Multigroup radiation diffusion; Pseudo transient continuation; Radiation-hydrodynamic codes with AMR

☆ This work was performed under the auspices of the U.S. Department of Energy by the University of California Lawrence Livermore National Laboratory under Contract No. W-7405-Eng-48.
* Corresponding authors. Tel.: +1 925 422 4213; fax: +1 925 423 9208.
E-mail addresses: shestakov@llnl.gov (A.I. Shestakov), soffner@berkely.edu (S.S.R. Offner).

0021-9991/$ - see front matter Published by Elsevier Inc.
doi:10.1016/j.jcp.2007.09.019

1. Introduction

This paper describes a numerical method to solve the radiation multigroup diffusion (MGD) equations. Two themes are presented. One is the scheme itself. We add pseudo transient continuation (Ψtc) to the familiar "fully-implicit" method of Axelrod et al. [2]. The second theme is code-specific. Our MGD solver is embedded in a multidimensional, massively parallel, Eulerian radiation-hydrodynamic code, which has patch-based, time-and-space Adaptive Mesh Refinement (AMR) capability. Our code's AMR framework stems from the Berger and Oliger idea [3] developed for hyperbolic, compressible hydrodynamic schemes. The idea was expanded by Almgren et al. [1] and applied to the type of elliptic solvers required for the incompressible equations of Navier–Stokes. Howell and Greenough [7] applied the Almgren et al. framework to the scalar, parabolic "gray" radiation diffusion equation, thereby creating the start of our radiation-hydrodynamic code.

The AMR framework works as follows. A domain, referred to as the "coarse" or L0 level, is discretized using a uniform, coarse spatial mesh size h_c.[1] After advancing with a timestep Δt_c, the result is scanned for possible improvement. One may refine subregions containing a chosen material, material interface(s), shocks, etc. Whatever refinement criteria are used, after the subdomains are identified, specific routines define a collection of "patches," which cover the subdomains. In two dimensions, the patches are unions of rectangles; in 3D, they are unions of hexahedra. The patches need not be connected, but they must be contained within the coarse level. The patches denote the "fine" or L1 level and are discretized with a uniform, spatial mesh size h_f. A typical refinement ratio h_c/h_f equals two, but higher multiples of two are also allowed.

Because the original framework was designed for temporally explicit hyperbolic schemes, Δt_c is restricted by a CFL condition. This implies a similar restriction for the L1 level timestep Δt_f. For the case, $h_c/h_f = 2$, level L1 time-advances twice using $\Delta t_f = \Delta t_c/2$. Boundary conditions for level L1 are supplied as follows. Wherever level L1 extends to the physical boundary, the level uses the conditions prescribed by the problem. Portions of level L1's boundary which lie inside the physical domain have conditions prescribed by time and space interpolated data obtained from the L0 solution. For diffusion equations, these conditions are of Dirichlet type. The numerical solution consists of both coarse and fine grid results. Unfortunately, as it stands, the composite solution does not guarantee conservative fluxes across the level boundaries. To maintain conservation, a separate procedure, dubbed a sync-solve (SS) is required. The SS reduces to an elliptic unstructured grid solve on the composite grid of L0 and L1 levels. The AMR procedure may be recursive. That is, a level L1 grid may generate its own subdomain for refinement, i.e., a level L2. In that case, one SS couples results from levels L1 and L2. Once the levels advance to the L0 level time, a SS coupling all three levels ensues. For the multigroup equations, the SS requires an unstructured grid solve for a coupled system of reaction-diffusion equations. Our scheme for a multigroup SS is an important theme of this paper.

The MGD equations stem from a discretization of the multifrequency radiation diffusion equations. The latter is an approximation to the equations of radiation transfer, obtained by assuming the matter to be optically thick, which suppresses the directional dependence of the radiation intensity. Details of the derivation may be found in various sources: Mihalas and Weibel-Mihalas [11], Zel'dovich and Raizer [25], Pomraning [16].

The gray radiation diffusion equation is a simplification of the MGD equations. It is essentially a one-group equation and is derived by integrating over all frequencies. Surprisingly, it gives very good results in many cases. However, it clearly cannot display frequency-dependent effects. When those are important, it gives incorrect results. Unfortunately, unless one solves a problem with both gray and MGD, one never knows when the former is adequate.

We now summarize the paper. Our MGD scheme consists of two parts. Sections 2 and 3 develop the level-solve algorithm, which is applied on each level. Section 2 develops the equations, the discretization, and our Ψtc scheme. Section 3 proves three lemmas which determine the initial magnitude of the Ψtc parameter σ. Our philosophy for σ is as follows. The result of the level solve is the time-advanced radiation group energy density, which physics dictates to be non-negative. Zeroing anomalously negative values is not an option since they are the correct conservative solution to the linear system that stems from the discretization of the system.

[1] In multiple dimensions, coordinates have their own mesh spacing.

Thus, the unphysical result nonetheless conserves energy. The difficulty is avoided if in the original formulation of the linear system $Ax = b$, A is an M-matrix and the right-hand-side (RS) is non-negative. Since we solve $Ax = b$ using an iterative scheme, the magnitude of σ is determined to ensure $b \geqslant 0$, a diagonally dominant A, and that the iterations converge. To a large extent, we are guided by Pert [15], who discusses how and why the solution to a discretization of an equation may be unacceptable from a physical standpoint. For a first reading, Section 3 may be skipped; the analysis of the required magnitude of σ is not needed for the subsequent sections.

We note that Ψtc is widely used to solve nonlinear systems of equations. It is closely related to the Inexact Newton Backtracking Method by Shahid et al. [17]. When applying Ψtc to a Newton solver, the basic idea is to limit the change to the iterates when one is far from the root but not restrict the change as one approaches the root. With Ψtc, limiting is done by the magnitude of the pseudo-timestep. Kelley and Keyes [8] put Ψtc on a solid analytic framework by examining the three regimes of Ψtc: small, medium, and large pseudo-timesteps. In the last regime, Ψtc recovers Newton's second order of convergence.

Our Ψtc implementation differs from the norm. Standard applications typically detect when a problem is "hard" and then reduce the timestep or some other parameter by an arbitrary amount. However, this method will not work for us because our solver is embedded in a time-dependent multiphysics code with separate modules for compressible gasdynamics, heat conduction, and radiation transport. Our MGD solver is called numerous times during the course of a simulation. (If running with AMR, it is called multiple times per physical time advance.) Although the physical Δt is controlled by various means, and depending on the problem can vary many orders of magnitude, we require a MGD solver that works under all conditions. Our Ψtc approach is similar to the one of Shestakov et al. [19]. We set the initial magnitude of the Ψtc parameter to ensure that for the first step, our iteration scheme converges and that the result is physical. We note that our usage of Ψtc is nearly equivalent to having the MGD module time-advance not in a single (physical) step Δt, but in smaller time increments until the desired time $t^0 + \Delta t$ is reached. Some colleagues refer to the process as "sub-cycling" the radiation module. It is easy to show that the lemmas of Section 3 still apply for sub-cycling.

Section 4 describes the second part of our solver, viz., the sync-solve. Section 5 contains results. Three problems are presented. The first, in Section 5.1, displays the accuracy of the method and its convergence properties: first order in time and second order in space. Section 5.2 demonstrates the utility afforded by Ψtc. For hard problems, it accelerates convergence; for very hard problems, Ψtc is indispensable. Section 5.3 models the explosive expansion of a hot metal sphere suspended in cold air. The simulation couples all of the code's physics modules. The problem is an ideal candidate for AMR since effects propagate a large distance away from the source, yet in early times, resolution is needed only near the sphere. The problem also demonstrates the necessity of multigroup diffusion. We find that if the sphere's energy is very high, gray diffusion gives the wrong answer. For a 1 MT energy source, our MGD simulation contradicts results of Brode [5], who used gray diffusion. Section 6 contains concluding remarks.

There are three appendices. Appendix A gives a table of exact values for the test problem described in Section 5.1. Appendix B discusses situations that may complicate attaining a diagonally dominant matrix when discretizing the multigroup system. Appendix C presents a spatial convergence analysis of the multigroup system when running in "production" mode, that is, with a dominant flux limiter and with AMR.

2. Level solve

Ignoring velocity terms and Compton scattering, the multifrequency radiation equations (CGS units) [11] are:

$$\partial_t u_\nu = \nabla \cdot D_\nu \nabla u_\nu + c\rho\kappa_\nu(B_\nu - u_\nu), \tag{1}$$

$$\rho\partial_t e = -c\rho \int_0^\infty \mathrm{d}\nu\ \kappa_\nu(B_\nu - u_\nu), \tag{2}$$

In (1) and (2), u_ν and e represent the spectral radiation energy density and matter specific energy, respectively. The former is a function of position x, time t and frequency ν, while e is a function of the mass density ρ and material temperature T, quantities which themselves depend on x and t. Evolution of ρ is governed by

hydrodynamics. Hence, in our context, ρ is a known function. Introducing the specific heat $c_v = \partial e/\partial T$ turns (2) into an evolutionary equation for T; hence, the left-hand-side (LS) becomes $\rho c_v \partial_t T$. The subscript v designates that the term varies with frequency. In (1) and (2), c denotes the speed of light, κ_v the absorption opacity, and B_v the Planck function,

$$B_v = (8\pi h/c^3)v^3/[\exp(hv/kT) - 1] \text{ (erg s cm}^{-3}),$$

where h and k are the Planck and Boltzmann constants, respectively. The diffusion coefficient D_v depends on the total inverse mean free path $\chi_v = \rho\kappa_v + \rho\kappa_{v,s}$, where κ_v and $\kappa_{v,s}$ are the absorption and scattering opacities, respectively. (The opacities are also functions of material composition, ρ and T.) In (1), the term $-D_v\nabla u$ denotes the spectral radiation energy flux. To limit energy streaming faster than c, a flux limiter is introduced, e.g.,

$$D_v = c/[3\chi_v + |\nabla(u_v)|/u_v]. \tag{3}$$

The multigroup equations are derived as follows. The frequency domain is discretized into G *groups* with boundaries $\{v_g\}_{g=0}^{G}$ satisfying

$$0 \leqslant v_0 < v_1 < \cdots < v_G < \infty.$$

The equations are integrated over groups. We define

$$u_g(x,t) = \int_g u_v = \int_{v_{g-1}}^{v_g} \mathrm{d}v\ u_v.$$

Time derivatives are replaced by differences and the system is multiplied by the timestep Δt. Integration of the transport and absorption terms requires defining group-averaged opacities. Linearizing the Planck function about a known temperature T^*, the absorption term is expressed as

$$\int_g \kappa_v(B_v - u_v) = \kappa_g[B_g + B'_g(T - T^*) - u_g],$$

where κ_g is the group-averaged absorption opacity, $B_g = \int_g B_v|_{T=T^*}$, and $B'_g = \int_g(\partial B_v/\partial T)|_{T=T^*}$. In a semi-implicit scheme, $T^* = T^0$, where T^0 is the temperature at the start of the time cycle. For fully-implicit differencing, we must iterate until T^* converges to T. For the transport term, we define

$$\Delta t \int_g \nabla \cdot D_v \nabla u = \nabla \cdot D_g \nabla u_g,$$

where D_g depends on a group-averaged inverse mean free path χ_g. Note that Δt has been absorbed into D_g.

The above definitions yield the multigroup equations,

$$0 = u_g^0 - u_g + \nabla \cdot D_g \nabla u_g + K_g(u,T), \quad g = 1,\ldots,G, \tag{4}$$

$$0 = \rho c_v(T^0 - T) - \sum_{\ell=1}^{G} K_\ell(u,T), \tag{5}$$

where u_g^0 and T^0 denote values at the start of the time-advance,

$$K_g(u,T) = a_g[B_g + B'_g(T - T^*) - u_g],$$
$$a_g = \Delta t c \rho \kappa_g.$$

Eqs. (4) and (5) comprise a nonlinear system with the strongest nonlinearity due to the emission term B. To a lesser extent, opacities also have a temperature dependence and for non-ideal gases, so does c_v. However, for ease of solution, we may choose to view (4) and (5) as a linear system in which case all coefficients are evaluated at the old temperature T^0. For simulations in which matter and radiation are tightly coupled, i.e., where we expect to have $u_v = B_v$, the solution to the semi-implicit difference equations is $u_g = B_g + B'_g(T - T^0)$, with B_g and B'_g evaluated at $T = T^0$. For high frequencies, $\lim_{v\to\infty}(B_v/B'_v) \sim 1/v$; hence, $B_g \ll B'_g$ for large g. Unfortunately, if the temperature is decreasing, i.e., if $(T - T^0) < 0$, the linearized emission term is negative for large

g, leading to the unphysical result: $u_g < 0$. On the other hand, if we are able to iterate on T^* so that it converges to T, then in tightly coupled simulations, we obtain the desired solution $u_g = B_g$ with B_g evaluated at the advanced temperature.

In our code we provide both options, i.e., solving a linear system, or converging on the implicit source.[2] In either case, solving (4) and (5) on a large domain with many groups presents a formidable task. To facilitate the task, we introduce pseudo transient continuation (Ψtc) and replace the zeros on the LS of (4) and (5) with the Ψtc derivatives,

$$\tau(u_g - u_g^*) \quad \text{and} \quad \rho c_v \tau (T - T^*),$$

where $\tau \geqslant 0$, the inverse of the pseudo-timestep, is the Ψtc parameter whose magnitude is at our disposal.

The variables u_g^* and T^* represent advances in pseudo-time; they always appear on the LS of (4) and (5). As mentioned above, we provide the option of running in either semi-implicit (SI) or fully-implicit (FI) mode. With SI, since B_g is linearized about $T = T^0$, in the definition of the coupling term K_g, we substitute T^0 for T^*. However for FI, K_g is defined as above; B_g is linearized about the pseudo-time temperature T^*. The two modes lead to subtle differences in the scheme, as shown below.

For the FI scheme, if the matter equation is solved for the temperature change, we obtain

$$\delta^{-1}(T - T^*) = \rho c_v (T^0 - T^*) - \sum_{\ell=1}^{G} a_\ell (B_\ell - u_\ell), \tag{6}$$

where

$$\delta^{-1} = \rho c_v \sigma + \sum_{\ell=1}^{G} a_\ell B'_\ell \quad \text{and} \quad \sigma \doteq 1 + \tau. \tag{7}$$

The domain of relevance $\tau \geqslant 0$ corresponds to $\sigma \geqslant 1$.

For the SI scheme, the temperature change is,

$$\delta^{-1}(T - T^0) = \rho c_v (\sigma - 1)(T^* - T^0) - \sum_{\ell=1}^{G} a_\ell (B_\ell - u_\ell). \tag{8}$$

The term δ is defined as above, but B_g and B'_g are evaluated at $T = T^0$.

For the FI scheme, if (6) is substituted into the equation for u_g, we obtain

$$-\nabla \cdot D_g \nabla u_g + (\sigma + a_g) u_g - f_g \sum_{\ell=1}^{G} a_\ell u_\ell = u_g^0 + (\sigma - 1) u_g^* + a_g B_g + f_g \left(\rho c_v (T^0 - T^*) - \sum_{\ell=1}^{G} a_\ell B_\ell \right), \tag{9}$$

where $f_g \doteq \delta a_g B'_g$. Eq. (7) implies $f_g < 1$, for all g. For the SI scheme, the RS of (9) changes: $\rho c_v (T^0 - T^*)$ is replaced with $\rho c_v (\sigma - 1)(T^* - T^0)$.

Eq. (9) corresponds to a linear system

$$\mathcal{A} u = w$$

of order $(N \times G)$, where N is the number of mesh cells and G the number of groups. The first term on the LS of (9) consists of second order, central differences over space. We write this term as

$$-\nabla \cdot D_g \nabla u_g = +\mathcal{D}_{d,g} u_g - \mathcal{D}_{o,g} u_g.$$

The first part represents multiplication of the vector u_g by a *diagonal* matrix; the second term denotes multiplication by the off-diagonal part. The coefficients of $\mathcal{D}_d$ and $\mathcal{D}_o$ are non-negative.

On the LS of (9), the term $-f_g \sum_{\ell=1}^{G} a_\ell u_\ell$ is referred to as the "re-emission source" [12], since it represents radiation energy absorbed by matter and re-emitted. If we define the *column* vectors f and a with components f_g and a_g, respectively, the re-emission term is expressed as the matrix–vector product

[2] At the time of this writing, opacities and c_v were time-lagged.

$$-(fa^{\mathrm{T}})u, \tag{10}$$

where $a^{\mathrm{T}} = \text{transpose}(a)$, and u is the column vector of unknowns. Since the re-emission term does not couple cells, (10) corresponds to separate products: one per cell, with each product of order G.

These observations allow expressing the matrix as

$$\mathcal{A} = \Lambda - M_1 - M_2, \tag{11}$$

where Λ is diagonal, M_1 contains the offdiagonal terms due to the (spatial) diffusion term, and M_2 contains the offdiagonal terms due to interfrequency coupling. The corresponding elements are

$$\Lambda_g = \mathcal{D}_{d,g} + \sigma + a_g - f_g a_g,$$
$$(M_1 u)_g = \mathcal{D}_{o,g} u_g,$$
$$(M_2 u)_g = f_g \sum_{\ell \neq g}^{G} a_\ell u_\ell.$$

The decomposition (11) leads to the iterative scheme proposed by Axelrod et al. [2], which improves a guess $u^{(i)}$ by successively solving

$$(\Lambda - M_2)u^{(i+1/2)} = w + M_1 u^{(i)}, \tag{12}$$
$$(\Lambda - M_1)u^{(i+1)} = w + M_2 u^{(i+1/2)}. \tag{13}$$

We solve (12) and (13) until $u^{(i)}$ converges. Convergence is gauged by evaluating the 1-norms of w and the residual $r = w - \mathcal{A}u$; the latter defined as,

$$r = w - \mathcal{A}u^{(i+1)} = M_2(u^{(i+1)} - u^{(i+1/2)}).$$

The procedure is fast since multiplication by M_2 is local to each cell, which is very convenient if the spatial domain is decomposed on multiple processors.

We now review the derivation of the system $\mathcal{A}u = w$. First, we assume that Ψtc is not used, i.e., that $\sigma = 1$ in (7) and (9). For the SI scheme, the terms B_ℓ and B'_ℓ are evaluated at $T = T^0$. For FI differencing, we require two types of iterations. Eqs. (12) and (13) comprise the *inner* iteration. It is initialized with $u^{(0)}$ equal to u^0. Once the inner iteration has converged to sufficient accuracy, (6) yields the new temperature. The SI scheme essentially ends after the inner iteration converges (see below). For FI differencing, after T is computed, the *outer* iteration sets $T^* = T$, recomputes B_ℓ and B'_ℓ at $T = T^*$ and returns to the inner iteration. The outer iteration halts when T^* converges.

If Ψtc is invoked, more care is required because when $\sigma > 1$, the system $\mathcal{A}u = w$ is not a true discretization of the multigroup equations. Despite this complication, Ψtc brings robustness to the scheme. The Ψtc parameter τ plays the role of an inverse timestep in pseudo-time. In principle, we could set τ to a large value and solve a succession of linear systems. The solution of each system represents an advance in pseudo-time. We continue advancing until we reach the pseudo-time steady-state. This is easily seen by letting $u_g^* = u_g$ on the RS of (9) and moving the term to the LS. However, making τ large is not practical as it involves many pseudo-time advances. Furthermore, the intermediate pseudo-time results are of no interest. Consequently, we adopt the strategy of making τ as small as possible. We discuss the strategy in Section 3.

Ψtc may be used with either SI or FI differencing. In the former, once (12) and (13) are converged, (8) yields the new temperature T. We then compute the 1-norm of the "nonlinear" residual of the linearized equation for the matter energy,

$$r_{nl} = V\left(\rho c_v(T - T^0) - \sum_{\ell=1}^{G} a_\ell[B_\ell + B'_\ell(T - T^0) - u_\ell]\right), \tag{14}$$

where V is the cell volume. The residual is compared with the 1-norm of the matter "energy" $V\rho c_v T$, and in order to monitor stagnation, it is also compared with the energy change over the pseudo-timestep $V\rho c_v(T - T^*)$. With FI, the temperature T, obtained from (6), is used to compute the emission B_ℓ. The residual r_{nl} is defined as in (14), except without the $B'_\ell(T - T^0)$ term.

Unfortunately, unless the iterations converge to round-off accuracy, energy may not be conserved. Lack of conservation stems from values of user-set parameters that control stopping criteria for the iterations. For example, it may be efficient to halt once $\|r_n\|_1 < 10^{-6}$, and the norm of the iterates $\|(\Delta T)/T\|_\infty < 10^{-2}$ since continuing brings little noticeable (visual) improvement to the solution. However, if one were to stop at that point, energy may not be conserved to desired accuracy. To restore conservation, we provide the option of an additional step. After the iterations stop, we assume that the last computed temperature T is "frozen" and use it to compute emission. In the SI scheme, emission into the gth group is defined as $S_g = B_g + B'_g(T - T^0)$, where B_g and B'_g are evaluated using T^0. (To prevent unphysical behavior, S_g is not allowed to be negative.) In the FI scheme, we evaluate B_g using T and set $S_g = B_g$. Having a known emission allows us to compute the energy-conserving radiation field. The groups decouple. For $g = 1, \ldots, G$, we solve

$$-\nabla \cdot D_g \nabla u_g + (1 + a_g)u_g = u_g^0 + a_g S_g.$$

After computing u_g, the matter energy density change is

$$\Delta\mathcal{E} = -\sum_{\ell=1}^{G} a_\ell (B_g - u_g),$$

where, if using the SI scheme, B_g is linearized about $T = T^0$, or with FI, is evaluated at T. The quantity $V\Delta\mathcal{E}$ represents the average energy change of the matter. In cells with more than one material, we adapt a suggestion of Zimmerman [27], which simulates intra-cell gray diffusion. The scheme assumes each material resides in its own sub-volume. We solve for separate, frequency-averaged radiation energy densities and matter temperatures in the sub-volumes. The energy change of the materials depends on the individual, frequency-averaged opacities as well as on $\Delta\mathcal{E}$.

We now briefly describe the spatial discretization. We largely follow procedures described by Howell and Greenough [7] (H&G) and Shestakov et al. [19]. Our MGD solver is embedded in an Eulerian radiation-hydrodynamic code with cell-centered fundamental variables: ρ,u_g, etc. The code has distinct 1, 2, and 3D executables; mesh cells are line intervals, rectangles, and rectangular hexahedra, respectively.

In 2 and 3D, we discretize the diffusion term $\nabla \cdot D_g \nabla\, u_g$ using the H&G subroutines since those are readily available. We note in passing that H&G use the Levermore-Pomraning flux limiter [9] instead of the simple expression in (3). For 1D we have our own discretization; $\nabla \cdot D_g \nabla u_g$ is written as

$$[D_{i+1/2}(u_{i+1} - u_i)/h - D_{i-1/2}(u_i - u_{i-1})/h]/h, \tag{15}$$

where the group index g is suppressed and where i is the cell index.

The *face*-centered diffusion coefficient $D_{i+1/2}$ is computed as follows. First, we modify (3) by adding the term β /h to the denominator, where β is a small, user-specified constant, e.g., 10^{-6}. After factoring h, we obtain

$$D = ch/[3\chi h + |\Delta(u)|/u + \beta],$$

where we suppress the group index and note that the expression is to be evaluated on a face. The denominator is now dimensionless. The second term is the relative difference of u; we discuss its discretization momentarily. The product χh is an optical depth. In this light, β provides a floor to the cell's optical depth. The aim is to avoid complications with the matrix solve in case $\chi \to 0$ and at the same time, u_v is nearly spatially constant, which may easily happen for high frequency groups. The face-centered opacity is an average of the adjoining cell-centered opacities. We offer several options. For the simulations in this paper, we typically use inverse averaging, but other options (arithmetic, square root) are also allowed.[3] The term $|\Delta(u)|/u$ is written as

[3] If the two opacities are very different, inverse averaging: $\kappa_{i+1/2} \doteq 2\kappa_i\kappa_{i+1}/(\kappa_i + \kappa_{i+1}) \to 2\min(\kappa_i,\kappa_{i+1})$. Assuming the opacity is monotone with T, the result is nearly the same as what is commonly done in gray diffusion, viz., forming a face-centered temperature, $T_{i+1/2} \doteq (T_i + T_{i+1})/2$, and calculating $\kappa_{i+1/2}$ directly with $T_{i+1/2}$. For example, if $\kappa = \kappa_0/T^n$ and $T_i \gg T_{i+1}$, inverse averaging gives $2\kappa_0/T_i^n$ while the face-centered T result is $2^n\kappa_0/T_i^n$. For the free-free gray opacity, $n = 3.5$; hence, the two results are similar. Of course, if the opacity is not monotone with T, the face-centered technique is better. We plan to incorporate that option in the future. However, we note that multigroup opacities are usually not strong functions of T.

$$2|u_{i+1} - u_i|/(u_{i+1} + u_i).$$

Other options are also available, e.g., instead of the arithmetic average, one may substitute max (u_{i+1},u_i) in the denominator. We plan to extend the above discretization to higher dimensions.

Cell-centered data, such as c_v, are obtained as in [7].

For coupling to the radiation field in mixed-material cells, we need averaged material properties, e.g., opacities. These are obtained by mass averaging. Suppressing the group index, if n is the material index and denoting averaging with an overbar, the opacity (cm^2/g) is given by $m\bar{\kappa} = \sum_n m_n\kappa_n$, where m_n is the mass of the nth material. Equivalently,

$$\bar{\rho}\bar{\kappa} \doteq \sum_n f_n\rho_n\kappa_n,$$

where $f_n \doteq V_n/V$ is the volume fraction.

This concludes the description of the algorithm used to advance the multigroup equations on an AMR level. In the following section, we analyze the convergence of (12) and (13), and we focus on how the Ψtc parameter σ ensures stable, robust iterations, to yield a physical, i.e., non-negative result.

3. Analysis of Ψtc

In this section we develop three criteria that set the Ψtc parameter. Disinterested readers can safely skip the analysis and continue to Section 4 where we discuss the implementation of the multigroup scheme in the context of AMR.

Recalling that $\sigma = 1 + \tau$, we develop lemmas that set the *initial* magnitude of τ, where by initial we mean the following. A new value of τ is determined at each time advance for each AMR level. The level advance consists of nested loops. For the "inner" iterations, τ is fixed. After convergence, τ is reset to $\tau \to \alpha_\tau\tau$, where α_τ is a user-set input whose default value is 1/2. Section 5.2 describes an experiment with another setting of α_τ. Our strategy for the initial τ is to ensure a non-negative w, diagonal dominance, and a convergent inner iteration. For the derivation, it is convenient to define

$$\mathcal{B} \doteq \sum_{\ell=1}^{G} a_\ell B_\ell, \quad \mathcal{B}' \doteq \sum_{\ell=1}^{G} a_\ell B'_\ell, \tag{16}$$

$$C'_g \doteq a_g B'_g/\rho c_v, \quad \mathcal{C} \doteq \mathcal{B}/\rho c_v, \quad \mathcal{C}' \doteq \mathcal{B}'/\rho c_v. \tag{17}$$

3.1. Positivity of w

Before analyzing the effect of Ψtc, we examine the scheme's behavior without it. If $\sigma = 1$, the term u_g^* disappears from (9). In the following discussion, we ignore the $T^0 - T^*$ term since for the SI scheme, or for the first FI inner iteration, $T^* = T^0$. Since $u_g^0 \sim B_g$, if either Δt is large or the coupling is strong, $a_g B_g \gg u_g^0$. Hence, in this case, the RS of the system, $w \approx a_g B_g - f_g\mathcal{B}$, where $\mathcal{B}$ is defined in (16). If $\sigma = 1$, $f_g = a_g B'_g/(\rho c_v + \mathcal{B}') = C'_g/(1 + \mathcal{C}')$. Hence,

$$w \approx a_g(B_g + B_g\mathcal{C}' - B'_g\mathcal{C})/(1 + \mathcal{C}').$$

Since $\mathcal{C}$ and $\mathcal{C}'$ are proportional to Δt times the opacity, the sole B_g term in the numerator is swamped by the other two terms when Δt is large or the matter is optically thick. In this limit, the sign of w equals the sign of $(B_g\mathcal{C}' - B'_g\mathcal{C})$, which may be negative.

However, with Ψtc, non-negativity of w is equivalent to the inequality

$$0 \leqslant p(\sigma) = u_g^*\sigma^2 + 2\tilde{b}\sigma + \tilde{c},$$

where

$$2\tilde{b} = u_g^0 - u_g^* + a_g B_g + \mathcal{C}'u_g^*,$$
$$\tilde{c} = \mathcal{C}'(u_g^0 - u_g^* + a_g B_g) + a_g B'_g[T^0 - T^* - \mathcal{C}],$$

for the fully-implicit (FI) scheme. The SI scheme, adds the term $a_g B'_g(T^* - T^0)$ to the definition of $2\tilde{b}$. If $\sigma = 1$, we recover the non-Ψtc scheme, which as shown, may have indeterminate sign(w). At the end of the section we show that the SI scheme is less robust. We first analyze the FI scheme.

For large σ, p is positive—even if $u_g^* = 0$. The derivative $\mathrm{d}p/\mathrm{d}\sigma$ increases monotonically and is positive for $\sigma = 1$. If $u_j^* = 0$, p increases linearly with σ and has slope $u_g^0 + a_g B_g > 0$. Hence, we have proved:

Lemma 1. *If* $p|_{\sigma=1} \geqslant 0$, *the* RS *of* (9) *is non-negative for all* $\sigma \geqslant 1$. *Otherwise*,

(1) *If* $u_j^* > 0$, *the* RS *of* (9) *is non-negative if*

$$\sigma \geqslant \sigma_{\min} = \max\left[\left(\sqrt{\tilde{b}^2 - u_g^*\tilde{c}} - \tilde{b}\right)/u_g^*\right].$$

(2) *If* $u_j^* = 0$, *the* RS *of* (9) *is non-negative if* $\sigma \geqslant \sigma_{\min} = -\max(\tilde{c}/2\tilde{b})$.

The lemma's limit is very restrictive for large Δt, as we now show. As $\Delta t \to \infty$, the terms a_g, $\mathcal{C}$ and $\mathcal{C}'$ dominate the definitions of $\tilde{b}$ and $\tilde{c}$. Hence,

$$\lim_{\Delta t\to\infty} 2\tilde{b} = a_g B_g + \mathcal{C}' u_g^*,$$
$$\lim_{\Delta t\to\infty} \tilde{c} = a_g B_g \mathcal{C}' - a_g B'_g \mathcal{C}.$$

Substituting into the expression for the root and factoring out $a_g u_g^*$ yields

$$\lim_{\Delta t\to\infty} \sigma_{\min} = \max \frac{a_g}{2}\left(\sqrt{(\alpha-\beta)^2 + 4\gamma} - (\alpha+\beta)\right),$$

where $\alpha = B_g/u_g^*$, $\beta = \sum_\ell \kappa_{\ell,g} B'_\ell/\rho c_v$, $\gamma = (B'_g/u_g^*)\sum_\ell \kappa_{\ell,g} B'_\ell/\rho c_v$ and $\kappa_{\ell,g} = \kappa_\ell/\kappa_g$. The term $a_g = c\Delta t \rho \kappa_g$ equals ℓ_c/ℓ_g, where ℓ_c is the maximum distance a photon can travel in time Δt and ℓ_g is the absorption mean free path for the gth group. We now show the remaining expression is of order one. If the radiation field is at equilibrium, $\alpha = 1$. The term B'_ℓ is of order B_ℓ/T. If it is exactly equal to B_ℓ/T, the expression multiplying $a_g/2$ vanishes.

If $u_g^* = u_g^0 = 0$ and $p|_{\sigma=1} < 0$, then for large Δt, $\sigma_{\min} \to (B'_g\mathcal{C} - B_g\mathcal{C}')/B_g$, which equals $c\Delta t$ times a term of order one.

We now consider the SI scheme. As noted above, SI adds the expression $a_g B'_g(T^* - T^0)$ to the definition of $2\tilde{b}$. Effectively, the extra term means that rather than having $2\tilde{b}$ depend on the emission source B_g (which is evaluated at T^*), the coefficient depends on the linearization $B_g + B'_g(T^* - T^0)$, with B_g and B'_g evaluated at T^0. If the temperature is decreasing the expression may be negative. As a consequence, we are not assured that $\mathrm{d}p/\mathrm{d}\sigma$ is positive. If u_g^* is non-zero, we can find a suitable σ. However, if $u_g^* = 0$, $p(\sigma)$ is a linear function with possibly a negative derivative. If that case arises as we query the cells, we set $\sigma = 1$ for the cell in question. Because of these uncertainties, by default, we run with the FI scheme.

3.2. Diagonal dominance

To prove diagonal dominance, we compute row sums. The diffusion terms sum to zero, since the matrix composed of just these terms must annihilate the vector $(1, 1, \ldots)$.[4] Thus, for diagonal dominance,

$$\sigma + a_g - f_g \sum_{\ell=1}^{G} a_\ell > d \geqslant 0.$$

Recalling the definition of f_g, the relation is equivalent to

$$0 \leqslant q(\sigma) = \sigma^2 + 2\tilde{b}\sigma + \tilde{c},$$

[4] In extreme cases, because of finite precision, the diffusion terms may swamp the other terms. We discuss the possibility in Appendix B.

where

$$2\tilde{b} = a_g + \mathcal{C}' - d,$$
$$\tilde{c} = a_g\mathcal{C}' - C'_g\sum_{\ell=1}^{G} a_\ell - \mathcal{C}'d,$$

and $\mathcal{C}'$, C'_g are defined in (17). As before, $\sigma \geqslant 1$ is the domain of interest. The quadratic $q(\sigma)$ is nonnegative for sufficiently large σ. However,

$$q|_{\sigma=1} = (1+\mathcal{C}')(1+a_g-d) - C'_g\sum_{\ell=1}^{G} a_\ell.$$

The a_g and $\mathcal{C}'$ terms are proportional to Δt. Hence, as $\Delta t \to \infty$, the sign of the expression is dominated by sign $(\mathcal{C}' - C'_g\sum_{\ell=1}^{G} a_\ell)$. Since the expression varies as $\sum_{\ell=1}^{G} a_\ell(B'_\ell - B'_g)$, the sign is indeterminate. However, $(dq/d\sigma)|_{\sigma=1}$ is positive for $d<2$. We have proved:

Lemma 2. *If $q|_{\sigma=1} \geqslant 0$ and $d>0$, $\mathcal{A}$ is strictly diagonally dominant for all $\sigma \geqslant 1$. Otherwise, $\mathcal{A}$ is strictly diagonally dominant if*

$$\sigma \geqslant \sigma_{\min} = \sqrt{\tilde{b}^2 - \tilde{c}} - \tilde{b}.$$

Remark 1. For large Δt,

$$\lim_{\Delta t\to\infty} \sigma_{\min} = \max\frac{a_g}{2}\left(\sqrt{(1-\beta)^2+4\delta} - (1+\beta)\right),$$

where $\delta = (B'_g/\rho c_v)\sum_\ell \kappa_{\ell,g}$ and, as before, $\beta = \sum_\ell \kappa_{\ell,g}B'_\ell/\rho c_v$, and $\kappa_{\ell,g} = \kappa_\ell/\kappa_g$. As in Lemma 1, when Δt is large, $\sigma_{\min} = \ell_c/\ell_g$ times a term which should be of order one.

3.3. Two-step iterative scheme

We have shown that for sufficiently large σ, $\mathcal{A}$ is an M-matrix. Hence, $(\Lambda - M_1) - M_2$ and $(\Lambda - M_2) - M_1$ are regular splittings, and each half of the two-step scheme (12) and (13) is a convergent iteration [24, Theorem 3.13, p. 89]. Here we analyze how the scheme reduces the error. Of particular interest is that for large Δt, the scheme (12) and (13) may *not* converge unless the ΨTC parameter σ is sufficiently large.

It is convenient to change variables,

$$v_j \doteq a_j u_j.$$

The system of interest is then $\mathcal{A}'v = w$, where

$$\mathcal{A}' = \Lambda - M_1 - M_2$$

and Λ is diagonal,

$$\Lambda_g = (\mathcal{D}_{d,g}/a_g) - f_g + 1 + \sigma/a_g,$$
$$(M_1 v)_g = \mathcal{D}_{o,g}v_g/a_g,$$
$$(M_2 v)_g = f_g\sum_{\ell\neq g}^{G} v_\ell.$$

If $\mathrm{e}^{(i)} = v - v^{(i)}$ defines the error for (12) and (13), the error satisfies

$$\begin{aligned}(\Lambda - M_1)\mathrm{e}^{(i+1/2)} &= M_2\mathrm{e}^{(i)},\\ (\Lambda - M_2)\mathrm{e}^{(i+1)} &= M_1\mathrm{e}^{(i+1/2)}.\end{aligned} \tag{18}$$

We express the error as a product of spatial and frequency components. For a 2D spatial domain,

$$\mathrm{e}^{(i)}_{k,m,g} = \epsilon^{(i)}_g \mathrm{e}^{\sqrt{-1}(k\theta_k + m\theta_m)}, \tag{19}$$

where the indices k and m refer to distinct spatial axes. We now analyze the iteration error

$$\mathrm{e}^{(i+1)} = (\Lambda - M_2)^{-1} M_1 (\Lambda - M_1)^{-1} M_2 \mathrm{e}^{(i)}.$$

Consider the unit vector $\hat{\mathbf{e}}_\ell$ consisting of N components, with unity in the ℓth position and zeros for the rest. Since the initial error $\mathrm{e}^{(i)}$ is a linear combination of such vectors, it suffices to analyze the case when the frequency component of $\mathrm{e}^{(i)}$ equals $\hat{\mathbf{e}}_\ell$. We will prove that for a properly chosen $\sigma \geqslant 1$,

$$||\mathrm{e}^{(i+1)}||_1 \leqslant \zeta < 1.$$

In other words, if σ is sufficiently large, one iteration of the two-step scheme reduces the error, which we will show occurs for $\zeta' < \zeta$, $\sigma(\zeta') > \sigma(\zeta)$. However, larger σ denote a smaller Ψtc time step, resulting in a longer pseudo-time to reach the desired steady-state.

Assuming that the diffusion coefficient does not vary in space[5] and that we use a uniform 2D spatial mesh with mesh size h, the error after the first half step is

$$\epsilon^{(i+1/2)}_g = f_g/[1 - f_g + (\sigma/a_g) + 2\eta_g(2 - \cos\theta_k - \cos\theta_m)], \tag{20}$$

where

$$\eta_g = D_g/a_g h^2 = l_{g,\mathrm{D}} l_{g,\mathrm{a}}/3h^2,$$

$l_{g,\mathrm{a}} = 1/\rho\kappa_g$ is the absorption mean free path, and $l_{g,\mathrm{D}}$ is the diffusion mean free path; the latter is the sum of the absorption and scattering opacities. In (20), the expression multiplying η_g is non-negative.[6] Since $f_g < 1$, $\epsilon^{(i+1/2)}_g$ is non-negative. Assuming the worst case $\theta = 0$ yields,

$$0 < \epsilon^{(i+1/2)}_g \leqslant f_g/(1 - f_g + \sigma/a_g), \tag{21}$$

a result which also holds in 1 and 3 dimensions. The bound is *sharp*; i.e., $\epsilon^{(i+1/2)}$ equals the bound if the original error $\mathrm{e}^{(i)}$ has no spatially varying component.

Since (19) holds for i, $i + 1/2$, and $i + 1$, we now analyze the second half step. In two dimensions,

$$M_1 \mathrm{e}^{(i+1/2)} = (\cos\theta_k + \cos\theta_m) 2\eta_g \mathrm{e}^{(i+1/2)}.$$

In $n = 1$, 2 or 3 dimensions, the parenthetical expression contains 1, 2 or 3 cosine terms. If we again assume $\theta = 0$, the expression is bounded by n.

To determine $\mathrm{e}^{(i+1)}$ from (18) we invert $(\Lambda - M_2)$ using the Sherman-Morrison formula by noting that

$$\Lambda - M_2 = \Lambda' - \mathbf{f}\mathbf{e}^{\mathrm{T}},$$

where $\mathbf{e}$ is the vector consisting of all ones, the components of $\mathbf{f}$ are the previously defined f_g, and Λ' is diagonal with

$$\Lambda'_g = \eta'_g + 1 + \sigma/a_g, \;\; \eta'_g \doteq 2n\eta_g. \tag{22}$$

In (22), we generalized by allowing for $n = 1$, 2, or 3 spatial dimensions. After some algebra, we obtain

$$|\epsilon^{(i+1)}_g| \leqslant \frac{1}{\Lambda'_g}\left[\eta'_g \epsilon^{(i+1/2)}_g + \left(\frac{f_g}{1 - \mathbf{e}^{\mathrm{T}}(\Lambda')^{-1}\mathbf{f}}\right)\sum_{\ell=1}^{G} \frac{\eta'_\ell \epsilon^{(i+1/2)}_\ell}{\Lambda'_\ell}\right],$$

where

$$1 - \mathbf{e}^{\mathrm{T}}(\Lambda')^{-1}\mathbf{f} = 1 - \sum_{\ell=1}^{G} f_\ell/\Lambda'_\ell. \tag{23}$$

[5] Since, as we show, the worst error arises for spatially constant error, we are free to ignore the diffusion flux limiter in the analysis.

[6] The corresponding expression in 1 and 3 spatial dimensions is also non-negative and bounded by 1.0 and 3.0, respectively.

Summing yields the 1-norm,

$$||\epsilon^{(i+1)}||_1 \leqslant \left[1 - \mathbf{e}^{\mathrm{T}}(\Lambda')^{-1}\mathbf{f}\right]^{-1} \sum_{\ell=1}^{G} \frac{\eta'_\ell \epsilon_\ell^{(i+1/2)}}{\Lambda'_\ell}.$$

Our task is done if we can show that the RS is bounded by ζ. Using (23) this entails showing that

$$\sum_{\ell=1}^{G} \frac{\eta'_\ell \epsilon_\ell^{(i+1/2)}}{\Lambda'_\ell} \leqslant \zeta\left(1 - \sum_{\ell=1}^{G} \frac{f_\ell}{\Lambda'_\ell}\right).$$

After substituting the bound (21) and simplifying, the inequality becomes

$$\sum_{g=1}^{G} \left(\frac{C'_g}{\Lambda'_g}\right)\left(\frac{\eta'_g}{1 - f_g + \sigma/a_g}\right) \leqslant \zeta\left[\sigma + \sum_{g=1}^{G}\left(\frac{C'_g}{\Lambda'_g}\right)(\Lambda'_g - 1)\right]. \tag{24}$$

To summarize, if (24) is satisfied the two-step scheme (12) and (13) converges and each iteration reduces the error by a factor ζ.

We now show that if Ψtc is not used, i.e., if $\sigma = 1$, and Δt is large, the scheme may not converge. If $\sigma = 1$, since $a_g \propto \Delta t$, $\lim_{\Delta t\to\infty} \Lambda'_g = \eta'_g + 1$ and $\lim_{\Delta t\to\infty} f_g = p_g$, where $p_g > 0$ and $\sum_g p_g = 1$. Also, if $\sigma = 1$, since $C'_g \propto \Delta t$, for large Δt, the lone σ on the RS of (24) is swamped by the sum. Dividing both sides of (24) by $c\Delta t$, the LS becomes

$$\sum_{g=1}^{G} \left(\frac{\rho \kappa_g B'_g \eta'_g}{\rho c_v (1 + \eta'_g)}\right)(1 - p_g)^{-1}.$$

On the other hand, if $\zeta = 1$, the RS tends to the same sum, but without the term $(1 - p_g)^{-1}$. This makes the LS larger than the RS, giving the desired contradiction. We have proved:

Lemma 3. *If $\sigma = 1$ and Δt is large, (12) and (13) may not converge.*

We now estimate how large to make σ in order to satisfy (24). The terms a_g and C'_g are proportional to Δt; also, $\sigma \geqslant 1$ and $\Lambda'_g > 1$. Hence, (24) holds for small Δt. To obtain a tractable expression, we derive a relation that stems from a more stringent inequality. Eq. (24) holds if we derive a σ that satisfies a relation insensitive to the lone σ on the RS and is obtained by requiring that the individual terms in the sum satisfy the inequality. This allows canceling the common term C'_g/Λ'_g. Hence, we seek σ satisfying

$$\eta'_g/(1 - f_g + \sigma/a_g) \leqslant \zeta(\Lambda'_g - 1).$$

Recalling that $f_g = C'_g/(\sigma + C')$ and using (22) leads to

$$0 \leqslant s(\sigma) \doteq \sigma^3 + \alpha_s\sigma^2 + \beta_s\sigma + \gamma_s,$$

where

$$\alpha_s = a_g(1 + \eta'_g) + C',$$
$$\beta_s = a_g[(1 + \eta'_g)C' - C'_g + a_g\eta'_g(1 - \zeta^{-1})],$$
$$\gamma_s = a_g^2\eta'_g[(1 - \zeta^{-1})C' - C'_g].$$

As before, $\sigma \geqslant 1$ is the domain of interest.

To simplify the analysis, we assume $\zeta = 1$, i.e., we seek a σ that guarantees marginal convergence. To this end, we define

$$\tilde{\beta}_s = a_g[(1 + \eta'_g)C' - C'_g],$$
$$\tilde{\gamma}_s = -a_g^2\eta'_g C'_g.$$

Consider the cubic

$$s(\sigma) = \sigma^3 + \alpha_s\sigma^2 + \tilde{\beta}_s\sigma + \tilde{\gamma}_s.$$

For $\sigma \geqslant 1$, all derivatives of s are positive. If

$$s(1) = 1 + \alpha_s + \tilde{\beta}_s + \tilde{\gamma}_s \geqslant 0,$$

then the scheme (12) and (13) converges. However, if $s(1) < 0$, we need a $\sigma > 1$ that renders $s \geqslant 0$. To avoid computing cubic roots, we approximate s by a quadratic $w(\sigma)$,

$$w(\sigma) = (3 + \alpha_s)\sigma^2 + (\tilde{\beta}_s - 3)\sigma + \tilde{\gamma}_s + 1,$$

and determine the root of w. The polynomials w and s and their first two derivatives agree at $\sigma = 1$. The difference $s(\sigma) - w(\sigma) = (\sigma - 1)^3$, i.e., $w(\sigma) < s(\sigma)$ for $\sigma > 1$. Hence, the positive root of $w(\sigma)$ overestimates the σ needed for marginal stability. We have proved:

Lemma 4. *If* $w|_{\sigma=1} \geqslant 0$, *the scheme (12) and (13) converges. If* $w|_{\sigma=1} < 0$, *the scheme converges if*

$$1 + \tau = \sigma \geqslant \sigma_{\min} = \frac{\sqrt{(\tilde{\beta}_s - 3)^2 - 4(3 + \alpha_s)(\tilde{\gamma}_s + 1)} + 3 - \tilde{\beta}_s}{6 + 2\alpha_s}.$$

4. Multigroup AMR scheme

In this section, we describe our implementation of AMR for the multigroup diffusion (MGD) system. The scheme necessarily adheres to the code's general architecture. That is, on each grid level each physics module (hydrodynamics, radiation) is called in order. These comprise the *level solves*. If AMR is used, the code refines in both space and time, as described by Howell and Greenough [7]. After a refined level is time-advanced to the next coarse level time, a synchronization is required in order to maintain conservation. For a scalar diffusion equation and only two levels, coarse and fine, the "sync-solve" is difficult enough since it reduces to effectively an unstructured grid solve over the combined coarse and fine grids. For MGD, the difficulty is compounded by having to sync-solve a coupled system of diffusion equations.

We begin by recalling the equations,

$$\partial_t u_g = \nabla \cdot D_g \nabla u_g + \kappa_g(B_g - u_g), \quad g = 1, \ldots, G, \tag{25}$$

$$c_v \partial_t T = -\sum_{g=1}^{G} \kappa_g(B_g - u_g), \tag{26}$$

where c_v is now the heat capacity, while D_g and κ_g are the diffusion and coupling coefficients. For ease of exposition, it is convenient to consider the one-dimensional case. The level solve module computes the solution to

$$u_{g,i} - u^0_{g,i} = (F_{g,i+1/2} - F_{g,i-1/2})/h_i + \gamma_{g,i}[B_g(T_i) - u_{g,i}], \tag{27}$$

$$c_{v,i}(T_i - T^0_i) = -\sum_{g=1}^{G} \gamma_{g,i}[B_g(T_i) - u_{g,i}], \tag{28}$$

where i is the cell index, $\gamma_{g,i} = \Delta t \kappa_{g,i}$, and $F_{g,i+1/2}$ is the fluence on the right edge of the ith cell,

$$F_{g,i+1/2} = \Delta t D_{g,i+1/2}(u_{g,i+1} - u_{g,i})/h_i.$$

For simplicity, assume there are only two levels, coarse and fine. Since (25) and (26) are reaction-diffusion equations, advanced with backward Euler temporal differencing, the discretization is unconditionally stable. Hence, in the following, in order to simplify the derivation, we assume that both levels are advanced with the *same* timestep. However, in the code we also time-cycle. If $i = 1, \ldots, N$ define the indices of all coarse-level cells, let $j = 1, \ldots, J$ define the indices of the refined cells and $i = I, \ldots, N$ define the indices of those coarse cells which are not refined. Coarse cells indexed with $i = 1, \ldots, I - 1$ are defined as the "covered" cells. We first update the entire coarse level, then the fine level. Both levels require boundary conditions (BC). The coarse level uses the user-specified BC. In the following example, the refined domain abuts the left side boundary and consists of J cells. Hence, the fine level uses the same BC on the left edge. The fine cell indexed with $j = J$ lies in the interior of the domain. We reuse the Howell and Greenough [7] infrastructure to provide a

Dirichlet condition for the cell. The datum is obtained by interpolating coarse grid data. Let k_j and h_i define the mesh widths of the fine and coarse cells, respectively. After multiplying by the mesh widths and summing over all cells and groups, we obtain

$$\sum_{j=1}^{J} k_j \left[c_{v,j}(T_j - T_j^0) + \sum_{g=1}^{G} (u_{g,j} - u_{g,j}^0) \right] + \sum_{i=I}^{N} h_i \left[c_{v,i}(T_i - T_i^0) + \sum_{g=1}^{G} (u_{g,i} - u_{g,i}^0) \right] = \sum_{g=1}^{G} (F_{g,N+1/2} - F_{g,1/2} - \delta F_{g,cf}), \tag{29}$$

where the last term is the fluence mis-match of the gth group at the coarse–fine interface,

$$\delta F_{g,cf} = F_{g,J+1/2} - F_{g,I-1/2}.$$

The AMR scheme assumes that the system is linear. Hence, the emission is expressed as

$$B_g(T_i) = B_{g,i}^{\bullet} + \acute{B}_{g,i}^{\bullet}(T_i - T_i^{\bullet}),$$

where $B_{g,i}^{\bullet}$ and its derivative with respect to T, i.e., $\acute{B}_{g,i}^{\bullet}$, are evaluated at a temperature $T_i^{\bullet}$, e.g., $B_{g,i}^{\bullet} = B_g(T_i^{\bullet})$. For semi-implicit Euler differencing, $T_i^{\bullet} = T_i^0$; if fully-implicit, $T_i^{\bullet} = T_i$. Either way, because $\delta F_{g,cf}$ need not be zero, (29) shows that energy may not be conserved after the two level advances. To restore conservation, we introduce the system for the corrections

$$u'_{g,i} = (F'_{g,i+1/2} - F'_{g,i-1/2})/h_i + \gamma_{g,i}[\acute{B}_{g,i}^{\bullet} T'_i - u'_{g,i}] + \delta F_{g,cf}/h_i, \tag{30}$$

$$c_{v,i} T'_i = -\sum_{g=1}^{G} \gamma_{g,i}[\acute{B}_{g,i}^{\bullet} T'_i - u'_{g,i}], \tag{31}$$

where $F'_{g,i\pm1/2}$ denote the implicit fluxes; they are functions of u'_g.

Eq. (30) holds for all groups $g = 1, \ldots, G$. In (30) and (31), the mesh index i varies over the coarse cells not marked for refinement ($i = I, \ldots, N$) as well as the fine cells ($j = 1, \ldots, J$). Following the methodology of [7], we put the fluence mis-match $\delta F_{g,cf}$ into the coarse cell(s) abutting the interface of the coarse and fine domains.

Summing the level advance and correction solutions yields conservation. If $u_{g,i}^* = u_{g,i} + u'_{g,i}$ and $T_i^* = T_i + T'_i$, combining (30) and (31) with (27) and (28), multiplying by the mesh widths, and summing over cells and groups, yields the desired conservation relation,

$$\sum_{j=1}^{J} k_j \left[c_{v,j}(T_j^* - T_j^0) + \sum_{g=1}^{G} (u_{g,j}^* - u_{g,j}^0) \right] + \sum_{i=I}^{N} h_i \left[c_{v,i}(T_i^* - T_i^0) + \sum_{g=1}^{G} (u_{g,i}^* - u_{g,i}^0) \right] = \sum_{g=1}^{G} (F_{g,N+1/2}^* - F_{g,1/2}^*).$$

Eqs. (30) and (31) present a formidable task as it requires solving a simultaneous system of equations for $(G+1)\overline{N}$ unknowns, where $\overline{N}$ denotes the number of refined cells plus the number of coarse cells not marked for refinement. The grid is effectively unstructured since it combines coarse and fine discretizations of the domain. We attack the problem by applying a variant of the "Partial Temperature" scheme [10,18]. In this scheme, groups are assigned a random order. As we cycle through the groups, each group computes a correction u'_g and a partial temperature T_g. Note the group index g for the temperature. Although the scheme decouples the groups from each other, the partial temperature T_g changes as we cycle through the groups. To be precise, for each group, we solve the system

$$u'_{g,i} = (F'_{g,i+1/2} - F'_{g,i-1/2})/h_i + \gamma_{g,i}[\acute{B}_{g,i}^{\bullet} T_{g,i} - u'_{g,i}] + \delta F_{g,cf}/h_i, \tag{32}$$

$$c_{v,i}(T_{g,i} - T_{g-1,i}) = -\gamma_{g,i}[\acute{B}_{g,i}^{\bullet} T_{g,i} - u'_{g,i}], \tag{33}$$

where, as above, the mesh index i ranges over all refined cells and all coarse cells not covered by the fine grid. For the group index g_1 that we first pick, $T_{g-1,i} = 0$ on the LS of (33). Solving (32) and (33) for $g = g_1$ yields the first partial temperature T_{g_1}. This temperature replaces $T_{g-1,i}$ on the LS of (33) for the second randomly picked group g_2. After cycling through the groups, the last one, g_G, gives the desired corrected temperature, i.e., $T'_i = T'_{g_G,i}$.

If (33) is summed over all g, the LS telescopes and we obtain,

$$c_{v,i}T'_i = -\sum_{g=1}^{G} \gamma_{g,i}[\acute{B}^{\bullet}_{g,i}T_{g,i} - u'_{g,i}].$$

Because we have $T_{g,i}$ on the RS instead of T'_i, this is not exactly (31). However, if $T_{g,i}$ does not vary too much as we cycle through the groups, the result is no worse than one obtained with the (commonly-used) partial temperature (PT) scheme since we apply PT to only corrections of the level-solve solution. Cycling through the groups in random order avoids biasing the deviation since the coupling in (32) and (33) may lower T for one group while raising it for another. In any case, the combined solution (u^*_g, T^*) is still conservative.

Eqs. (32) and (33) are solved using a Schur complement. Since (33) does not involve spatial derivatives, we can easily solve for $T_{g,i}$. After substituting the result into (32), we obtain a single scalar equation for $u'_{g,i}$, albeit now, on the unstructured grid composed of coarse and fine cells, viz.,

$$u'_{g,i} = (F'_{g,i+1/2} - F'_{g,i-1/2})/h_i + \gamma_{g,i}\eta_{g,i}[\acute{B}^{\bullet}_{g,i}T_{g-1,i} - u'_{g,i}] + \delta F_{g,cf}/h_i,$$

where, $\eta_{g,i} = c_{v,i}/(c_{v,i} + \gamma_{g,i}\acute{B}^{\bullet}_{g,i})$. After solving for $u'_{g,i}$, Eq. (32) yields $T_{g,i}$. The fluence mis-match $\delta F_{g,cf}$ acts as a source to the corrections. For groups with long mean free paths (mfp) and weak coupling, $\delta F_{g,cf}$ diffuses over the mesh. For groups with short mfp and strong coupling, $\delta F_{g,cf}$ is spread locally over the group energy $u'_{g,i}$ and "absorbed" into the matter.

Before closing this section, we note an inconsistency in the above *multilevel* scheme, indeed in any scheme embedded in a multiphysics code like ours, which advances several modules (hydrodynamics, heat conduction, radiation) using operator splitting. With splitting, on each level, the modules are advanced in order. For simulations using hydrodynamics and radiation diffusion and running with coarse L0 and fine L1 levels, the order of operations is as follows. Level L0 first advances hydrodynamics, then radiation. Next, if refining by a factor of two, L1 advances in the order: hydrodynamics, radiation, hydrodynamics, radiation. The multilevel solve advances in the same order: hydrodynamics, then radiation. This implies that the radiation multilevel solve uses coefficients, e.g., ρ, that are not the same as those used by the radiation level solve modules. In principle, one cannot simply add the correction equations to the level solve equations and claim that the sum satisfies a consistent set of equations. Nonetheless, the solution remains conservative.

5. Simulations

This section presents results using the multigroup scheme. We consider three problems. In Section 5.1, we present a test problem with a known analytic solution. We compare numerical results with tabular data, previously published by Shestakov and Bolstad [21]. Using Richardson extrapolation, we show that our Ψtc scheme, i.e., what we apply on a level, is second (first) order correct in space (time). When running with AMR, the temporal accuracy is first order. Accuracy of the spatial order depends on the norm used to measure convergence. In the most stringent ∞-norm, the order degrades to first, or worse, as shown at the end of Section 5.1. Section 5.2 develops a variation of the Section 5.1 test problem in order to demonstrate the benefits brought by Ψtc. We do this by running with and without Ψtc. We make several runs, each for only one timestep. Runs are made with successively larger Δt. Because of fully-implicit differencing, as $\Delta t \to \infty$, the numerical solution should approach the time-independent, steady-state. The problem in Section 5.3 brings everything together. We simulate the explosive expansion of a metal sphere suspended in air. The expansion is due to sourcing a large amount of energy in a short time into the sphere. Simulations are done with the code's full functionality, i.e., we couple all of the physics modules and also use AMR.

5.1. Linear MGD test problem

In this section we present results for a MGD problem with a known solution. Due to the nonlinearity of the equations, there are no test problems with analytic solutions. Thus, to validate and verify our algorithm, we consider the linearized multigroup equations developed by Shestakov and Bolstad (S&B) [21] and compare with tabular data.

The S&B tables present results for a 64-group discretization of the linearized, non-dimensional, multifrequency diffusion equations derived by Hald and Shestakov (H&S) [6]. In the following, we briefly derive the non-dimensional system, describe the test problem, explain how to set up the problem in a radiation-hydrodynamic code, demonstrate the problem's relevance to typical applications of multigroup diffusion, compare results with an improved-accuracy table [4] (supplied in Appendix A), and conclude by proving that our multigroup scheme's convergence is first order in time and second order in space.

The nonlinear multifrequency H&S system is derived by assuming slab symmetry, constant density, an ideal gas EOS, and an opacity characteristic of free-free transitions. One advantage of the H&S system is its non-dimensional form, which enables comparing results from codes using different dimensional units. The equations are obtained by choosing characteristic values for density ρ_0, temperature T_0, and inverse mean free path (mfp) $\kappa = \kappa_0/\nu^3$ with $\kappa_0 = \text{const}$ and ν the frequency variable. Radiation emission is given by a Wien distribution,[7] i.e., $B_W = B_0\nu^3\exp(-h\nu/kT)$, where $B_0 \doteq 8\pi h/c^3$ is the same constant defining the Planck function. The inverse mfp appears in both the diffusion, $D = c/3\kappa$, and the radiation-matter coupling terms, $c\kappa$. (The diffusion is *not* flux limited.) The normalization proceeds as follows. The values ρ_0, κ_0, and T_0 define the other normalization constants,

$$v_0 \doteq kT_0/h, \quad \ell_0 \doteq v_0^3/\kappa_0, \quad x_0 \doteq \ell_0/\sqrt{3},$$
$$t_0 \doteq \ell_0/c, \quad u_0 \doteq B_0 v_0^3, \quad E_0 \doteq u_0 v_0.$$

By defining non-dimensional variables, $x' = x/x_0$, $t' = t/t_0$, $u' = u/u_0$, $\nu' = \nu/\nu_0$, etc., (and dropping the primes) we obtain the normalized system,[8]

$$\partial_t u = \nabla\cdot\nu^3\nabla u + (\nu^3 e^{-\nu/T} - u)/\nu^3, \tag{34}$$

$$R\partial_t T = -T + \int_0^\infty (u/\nu^3)\,d\nu, \tag{35}$$

where the constant

$$R = (h/k)(\rho_0 c_v/u_0)$$

and c_v is the specific heat. Henceforth, unless stated otherwise, we use non-dimensional variables.

The H&S system yields a precise definition of the multigroup equations since the group integrals can be computed exactly, an impossible task for definite integrals of the Planck function. Given a group structure $\{\nu_g\}_{g=0}^G$, after integrating over groups,

$$\partial_t u_g = \bar{\nu}_g^3\partial_{xx}u_g + p_g T - u_g/\bar{\nu}_g^3, \quad g = 1,\ldots,G, \tag{36}$$

$$R\partial_t T = -T + \sum_{g=1}^G u_g/\bar{\nu}_g^3 \tag{37}$$

where $u_g = \int_g u\,d\nu$ and $\bar{\nu}_g$ is a group's representative frequency. S&B define $\bar{\nu}_g$ as $\sqrt{\nu_g\nu_{g-1}}$ and $\bar{\nu}_1$ as $\nu_1/2$ since the lowest group boundary is zero. The emission coefficients are

$$p_g \doteq \exp(-\nu_{g-1}/T) - \exp(-\nu_g/T). \tag{38}$$

If the group structure is broad enough, $\sum_g p_g = 1$.

Eqs. (36) and (37) are *nonlinear* because of the product $p_g T$. To derive an analytic solution, S&B follow the approach of Su and Olson [22,23], which requires a *linear* system since it uses Fourier and Laplace transforms. S&B linearize by defining a *fixed* temperature T_f and substituting T_f for T in (38).

Except for one item, it is easy to assemble the S&B linearized MGD system in a conventional radiation-hydrodynamic code. Such codes usually allow an ideal gas EOS and a desired analytic form for the opacity.

[7] It is noteworthy that H&S's choice of opacity and Wien spectrum for B gives the same emission source κB_W as would be obtained by including stimulated emission (SE) effects [25] and using the Planck function, since SE multiplies κ by the factor $(1 - e^{-h\nu/kT})$. Also note that without SE, the resulting Planck-averaged gray opacity does not exist; the integral diverges.

[8] If instead of B_W, H&S had used the Planck function, the factor $e^{-\nu/T}$ in Eq. (34) would be replaced by $(e^{\nu/T} - 1)^{-1}$. However, H&S would then be unable to form Eq. (35), since the integral over all ν (the total emission) diverges—see prior footnote.

One chooses arbitrary values for ρ_0, κ_0, T_0, and picks a specific heat c_v to set R. In our simulations, $\rho_0 = 1.8212111 \times 10^{-5}$ g cm^{-3}, $T_0 = 0.1$ keV, and $\kappa_0 = 4.0628337 \times 10^{43}$ cm^{-1} s^{-3}. To comply with S&B, we chose c_v to obtain $R = 1$. Our ρ_0, T_0, and κ_0 choices were dictated purely by reasons of convenience. Since we compare with a non-dimensional result, other constants may be used instead.

The subtle item is how to force a code's spectral emission rate to equal $p_g(T_f)T$. We accomplish the task as follows. The gth group's emission is $a_g[B_g + B'_g(T - T^*)]$, where $a_g = \Delta t c \rho \kappa_g$ and κ_g is the group-averaged opacity. The terms B_g and B'_g are integrals over the gth group, at temperature T^*, of the Planck function and its derivative w.r.t. T. The integrals are computed by a FORTRAN subroutine, which takes T^* as an input variable. For the test problem, we use a different subroutine, which when called, first defines

$$B'_g = (\bar{v}_g v_0)^3 (8\pi k/c^3)[\exp(-y_{g-1}) - \exp(-y_g)],$$

where $y_g = h v_g v_0 / kT_f T_0$. After computing B'_g, the routine sets $B_g = B'_g T^*$. In the y_g definition, v_g and T_f are non-dimensional, while v_0 and T_0 are the normalization constants. The $(\bar{v}_g v_0)^3$ term cancels the $1/v^3$ dependence of the opacity.

For the test, we consider S&B's problem 1. The non-dimensional domain is $0 < x < X$, where we set $X = 4$. The initial condition is $T = 1$ (0) for $x < (>) 0.5$ and $u = 0$ everywhere. We use symmetry boundary conditions at $x = 0$ and homogeneous Milne at $x = X$, i.e., $u_g + (2\ell_g/3)\partial_x u_g = 0$, where ℓ_g is the mean free path. We use the same group structure as S&B: 64 groups, starting at zero, with widths increasing geometrically by the factor 1.1. We set $v_1 = 5 \times 10^{-4}$ as the width of the first group.[9] The test simulates an initially hot slab of material encased by cold matter. Since u is initially zero throughout, the solution evolves by first coupling in the hot subdomain. As radiation diffuses out, it couples to cold matter thereby heating it. Because of the opacity's $1/v^3$ dependence, the group's diffusion and coupling rates differ.

Although the problem appears contrived, it represents effects of radiation diffusion. We prove the assertion in Fig. 1 where we display the temperature T and the total radiation energy density E_r $(= \sum_g u_g)$ for two simulations ending at $t = 1$. Solid lines pertain to the linearized system, where $T_f = 1.0$. Dashed lines are solutions of the "physical" nonlinear MGD system using Planckian emission. The similarity of the solutions validates the relevance of the test problem. We used $T_f = 1.0$ (instead of S&B's $T_f = 0.1$) because over the short duration of the simulation, the emission temperature in the hot subdomain is of order 1.0 rather than 0.1.

We now present our MGD result using S&B's parameter $T_f = 0.1$. Table 1 displays the relative errors of T and E_r for various x, at $t = 1.0$. For a variable f, we define the error $\varepsilon(f) = |(f_x - f_k)/f_x|$, where f_k are our numerical results and f_x are the S&B table values, listed in Appendix A.[10] Table 1 shows that we obtain better than 0.5% accuracy over the domain $0 \leqslant x \leqslant 1$. The worst error 0.48% occurs for T at $x = 0.51$. At that point, according to the table in Appendix A, T undergoes more than a 20-fold drop from its value at $x = 0.49$. We focus attention at the domain near $x = 0.5$ since that is where the variables undergo the sharpest change. At these points, we obtain better than 0.1% errors, except for T at $x = 0.52$ and 0.53. Errors near $x = 1.0$ are less important for two reasons. First, the S&B domain extends to infinity while ours extends to only $X = 4$. Hence, for large x, our results become less accurate.[11] Second, our code requires having a positive min (T). Hence, we cannot initialize with $T = 0$ in the cold region. At the end of the run, at $x = 1$, our temperature has risen by only a factor of 10^4, which precludes reaching much better than 0.1% accuracy there.

We were unable to use the S&B tables for a convergence study to verify our scheme's convergence properties w.r.t. timestep Δt and mesh size h. We speculate that the reason is that the truncation is a mix of errors due to finite Δt and h. Hence, a refinement study of one may be polluted by an overly coarse value for the other. However, we can use Richardson extrapolation to prove that our scheme is correct to first order in time and second order in space. Let v_k denote a numerical solution to an equation discretized by a constant parameter k. For an initial value ODE, k represents the timestep; for a time independent equation, k is the mesh width. If v is the analytic solution,

[9] A misprint in [21] erroneously has $v_1 = 10^{-4}$.

[10] For each point, f_k is the arithmetic average of the two adjoining cell-centered values.

[11] When we compare results of two simulations at the cells adjoining $x = 1.0$ where one run uses $X = 4$ and for the other, $X = 8$, we find the relative differences: 8×10^{-6}, 2×10^{-7} for E_r, T, respectively. Since these differences are 3–4 orders of magnitude less than Table 1 errors at $x = 1.0$, increasing the domain beyond $X = 4$ would have little impact on the entries of Table 1.

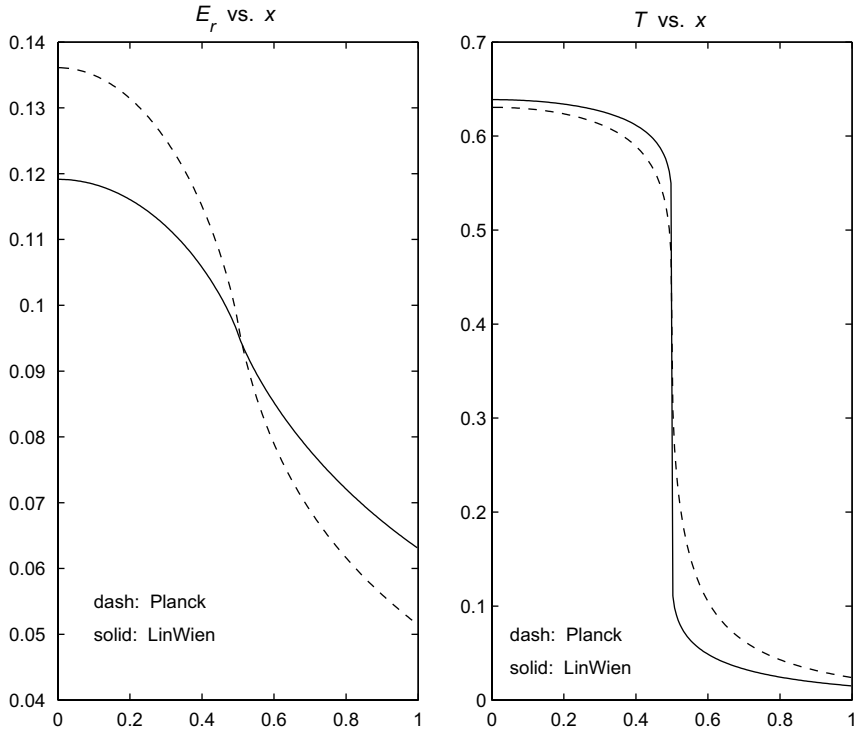

Fig. 1. Linear MGD test. Comparison of the linear solution ($T_f = 1.0$) with the solution of the nonlinear MGD system with Planckian emission; $t = 1$.

Table 1
Linear MGD test. Relative errors times 1000

x	$\varepsilon(T) \times 10^3$	$\varepsilon(E_r) \times 10^3$	x	$\varepsilon(T) \times 10^3$	$\varepsilon(E_r) \times 10^3$
0.00	0.0016	0.3012	0.51	4.8468	0.2785
0.20	0.0015	0.3028	0.52	1.8220	0.0031
0.40	0.0005	0.3268	0.53	1.0528	0.1293
0.46	0.0081	0.3903	0.54	0.7320	0.2128
0.47	0.0174	0.4252	0.60	0.3316	0.5263
0.48	0.0467	0.4945	0.80	0.6099	1.3841
0.49	0.2205	0.6979	1.00	1.4253	2.2138
0.50	0.0019	0.3518			

Numerical result obtained with $T_f = 0.1$, $h = 1/400$, $\Delta t = 1/200$.

$$v_k = v + \alpha k^a + \mathcal{O}(k^b),$$

where $0 < a < b$, and where α is independent of k.

In the asymptotic regime, the k^a term dominates the error, which allows ignoring the $\mathcal{O}(k^b)$ term. Assuming we have three solutions v_k, v_{2k}, v_{4k}, a ratio of differences yields

$$\frac{v_{2k} - v_{4k}}{v_k - v_{2k}} = 2^a.$$

The order of convergence a is found by taking logarithms.

We apply this procedure to estimate the orders of convergence. First, for the Δt study, we fix $h = 0.01$ and obtain three results using $k = 0.5 \times 10^{-8}$ s, $2k$ and $4k$. For the Δx study, we fix $\Delta t = 0.5 \times 10^{-8}$ s and use $k = 0.0025$. In both studies, runs are halted when $t = t_0$. We compute a at 15 points across the domain $[0, 1]$ for both E_r and T and focus attention at $x = 0.5$, where the fields undergo the sharpest change. Results

are presented in Fig. 2. The left plot clearly displays first order temporal convergence since $a \approx 1$ across the domain. The right plot supports our contention of second order spatial convergence. The low $a \approx 1.82$ (1.89) values for E_r (T) arise only at the two points $x = 0.49$, 0.51. We claim that at these points, we are not yet in the asymptotic regime.

The results of Fig. 2 pertain to a solution obtained on a single level, i.e., without using AMR. We now analyze how AMR affects the order of spatial and temporal convergence. For each study, Δx and Δt, we make three simulations (as before, we halt at $t = 1.0$) in order to apply our Richardson extrapolation technique. In each study, the composite grid consists of a "base" level L0 mesh over the entire domain and two AMR levels. Each level refines by a factor of two. Both L1 and L2 levels refine around $x = 0.5$. We examine convergence at points x in *all levels*.

For the Δt study, all three runs use the same composite spatial mesh. We make three runs; each with fixed timesteps Δt_0, $2\Delta t_0$ and $4\Delta t_0$, where $\Delta t_0 = 1/400$. The composite mesh uses $\Delta x = 1/100$ on level L0. The L1 mesh extends over $0.36 \leqslant x \leqslant 0.64$, and the L2 mesh extends over $0.42 \leqslant x \leqslant 0.58$. We obtain nearly the same temporal order as for the level solve. Fig. 3 displays a for the 128 cells on $0 < x < 1$. The lowest order, $a \approx 0.94$, occurs at $x = 0.38$ (0.62) for E_r (T) near the L0 and L1 coarse–fine interface.

The Δx study requires more care. For each run, the L1 mesh extends over $0.25 \leqslant x \leqslant 0.75$, and the L2 mesh extends over $0.375 \leqslant x \leqslant 0.625$. We refer to the three runs as R1, R2 and R4, where R1 and R4 use the "coarsest" and "finest" composite grids, respectively. For the three runs, the level L0 mesh sizes are 1/40, 1/80 and 1/160, respectively. Because each AMR level refines by a factor of two, for R1, the L0, L1 and L2 mesh sizes are also 1/40, 1/80 and 1/160. The R2 mesh widths are 1/80, 1/160, and 1/320; R4's are 1/160, 1/320 and 1/640. The composite grids are constructed so that within each level, the R1 cell boundaries are also cell boundaries of runs R2 and R4. Hence, by arithmetic averaging adjoining cell-centered data, we obtain numerical results at the same points for each run. These (averaged) values are used for Richardson extrapolation. Fig. 4 displays the ratio $(f_{R2} - f_{R1})/(f_{R4} - f_{R2})$ for the 79 faces on $0 < x < 1$. The ratio is approximately 4 over most of the domain, which indicates second order convergence. However at the coarse–fine interfaces, the order drops significantly; especially for T at $x = 0.25$ and 0.375.

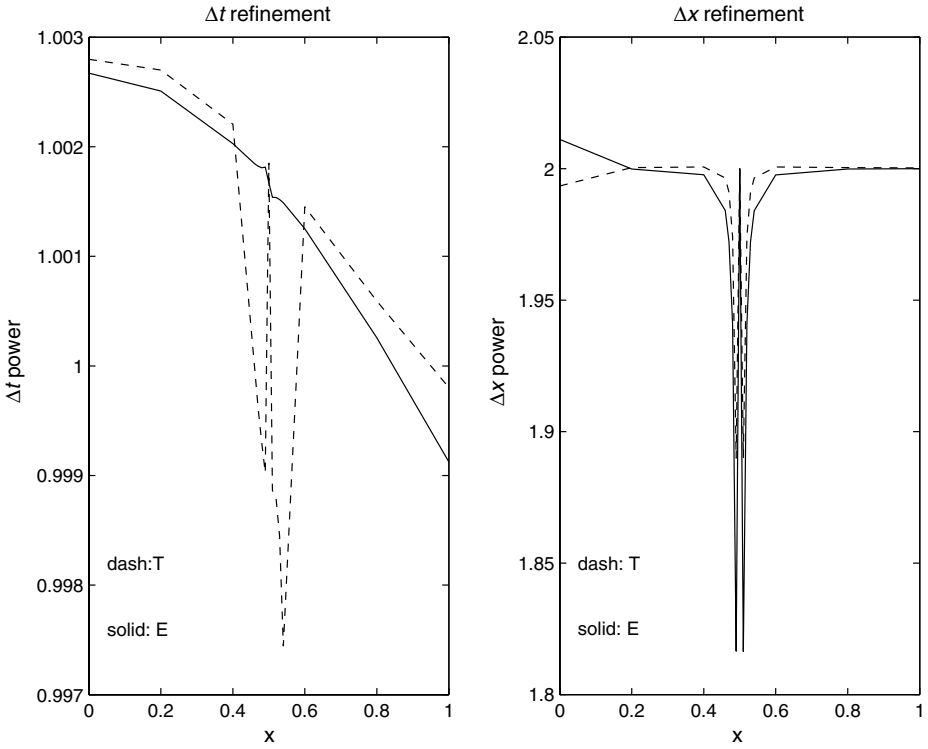

Fig. 2. Timestep and meshsize orders of convergence; Δt (Δx) on left (right) sides; $t = 1.0$; see text.

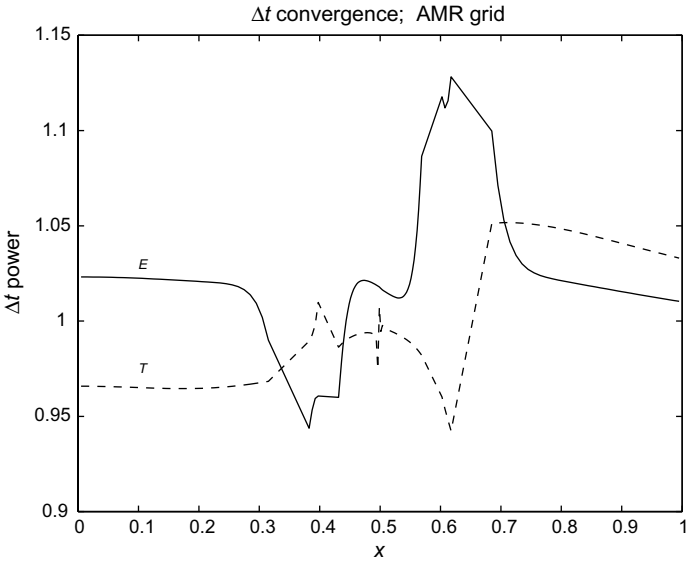

Fig. 3. Timestep order of convergence on composite AMR mesh; see text.

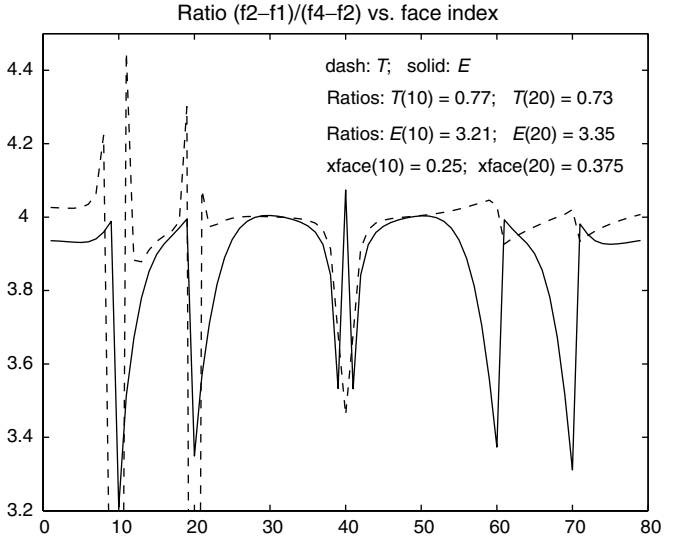

Fig. 4. Meshsize order of convergence on composite AMR mesh; see text.

The loss of accuracy at the coarse–fine (C–F) interfaces is due to the discretization of the diffusion operator. We use the infrastructure developed by Howell and Greenough [7] to assemble the linear systems. Unfortunately, the difference stencils—which are not discussed in detail in [7]—have a shortcoming near the interface. A more accurate discretization would yield an asymmetric matrix; for reasons of efficiency, symmetric linear solvers were preferred.

The inaccuracy can be analyzed by considering a derivative such as u_{xx} near the C–F interface. Assume that level L0 lies to the left of L1. For $i = 0, 1, 2$, let x_i denote the first three cell centers on L1 and let h define the L1 mesh size. Let x_c denote the center of the coarse cell next to the C–F interface. On L1 interior points, e.g., on x_1, u_{xx} is approximated by the difference: $(u_0 - 2u_1 + u_2)/h^2$. Hence, $1/h^2$ is the off-diagonal matrix coefficient corresponding to u_0 on the x_1 row. For the matrix to remain symmetric, the u_1 coefficient on the x_0 row must equal $1/h^2$. At x_0, u_{xx} is written as a difference of the right and left fluxes divided by the cell width h. The right

flux is $(u_1 - u_0)/h$. The left flux is expressed as the difference $(u_0 - u_c)$ divided by the distance between the cell centers. If L1 refines by a factor of two, the distance $x_0 - x_c = 3h/2$. Thus, at x_0, to maintain symmetry, u_{xx} is approximated by

$$\left(\frac{u_1 - u_0}{h} - \frac{u_0 - u_c}{3h/2}\right)/h.$$

Unfortunately, the left flux is not centered on L1's left-most face (at $x = x_0 - h/2$). A Taylor expansion shows that the difference is inconsistent; it equals $(5/4)u_{xx} + \mathcal{O}(h)$ and this is the source of the error. However, the error is localized. In a global sense, it is $\mathcal{O}(h)$, when computed by integrating over the entire domain: $\int u_{xx}\,dV$. This concludes the refinement study on an AMR mesh.

To summarize, in this section we have shown: (a) With a proper choice of T_f, the test problem mimics MGD physics. (b) We obtain excellent agreement with the S&B tables. (c) Our scheme is correct to first order in time and second order in space. (d) On an AMR mesh, the scheme incurs the same loss of accuracy as the one presented by Howell and Greenough [7] since we use the same discretization at coarse–fine interfaces.

5.2. Benefits of Ψtc

We now present results that illustrate the benefits obtained by using Ψtc. We show that for sufficiently large Δt, the conventional (ADR) scheme of Axelrod et al. [2] i.e., where $\sigma = 1$, fails to converge. Furthermore, if Δt is only moderately large, so that the ADR scheme does converge, introducing Ψtc accelerates convergence.

We begin by considering a variation of the problem introduced in Section 5.1. In this section, unless stated otherwise, we use normalized variables. First, we replace the Wien distribution with the Planck function. After normalizing, we obtain an equation similar to (34) except that $e^{-\nu/T}$ is replaced by $(e^{\nu/T} - 1)^{-1}$. Without stimulated emission effects, the *multifrequency* system is ill posed since the RS of the temperature equation integrates the coupling term over all ν. (The integral of B_ν/ν^3 diverges.) Since this is only a test, we ignore this complication. We use seven geometrically spaced groups, whose widths double with increasing frequency. The leftmost group boundary is zero; the first group width $\nu_1 = 0.5$; the last boundary $\nu_7 = 63.5$. As in Section 5.1, the first group's opacity is evaluated at $\nu_1/2$ and the rest are evaluated at the square root average. The spatial domain is $0 < x < 2$. The initial conditions are as before, viz., $T = 1$ (0) for $x <$ (>)0.5 and u is initially zero. We impose symmetry boundary conditions on both left and right endpoints. Hence, at all times, the total energy should equal the initial amount $\int_0^{1/2} RT\,dx = 1/2$.

Our test consists of several runs, each for only one timestep. All runs use $h = 0.01$. We run in fully-implicit mode; hence, upon convergence, the temperature T and emission source $B_\nu(T)$ are consistent. For infinitely large Δt, a single time advance yields the steady-state with $T = T_r$, where the radiation energy $E_r = aT_r^4$. In the non-dimensional system, since B_ν is the Planck function, $a = \pi^4/15$. Hence, the equilibrium temperature is the solution to,

$$2(T_e + aT_e^4) = 1/2, \quad \text{i.e.,} \;\; T_e = 0.2314.$$

The Ψtc result, where $\Delta t = 1000$, is displayed in Fig. 5. The figure shows that the two fields are nearly in equilibrium and almost spatially constant; T_r and T vary less than 1% and 2.4% respectively. The initially high T in $x < 0.5$ has decayed more than fourfold. The radiation field, as it coupled in the initially hot region, diffused outwards thereby heating the cold region.

The simulations were run with and without Ψtc. Both runs consist of nested "inner" and "outer" loops. The inner iterations (12) and (13) progress until the residual and the iterate difference $\|u^{(i+1/2)} - u^{(i)}\|$ fall below specified tolerances (which may not happen). At that point, the outer iteration computes a revised temperature T using (6). We then reset $T^* = T$ and use it to recompute the B_ℓ and B'_ℓ coefficients. For the first outer iteration, $T^* = T^0$. The iterations conclude when the temperature change and the nonlinear residual fall below their specified tolerances.

The problem's difficulty increases with Δt. Without Ψtc, it becomes impossible to solve if Δt is very large because of the computer's finite precision. For large Δt, the time derivatives, e.g., $(u - u^0)/\Delta t$, are dominated by the other terms. Hence, the initial condition (u^0, T^0) becomes less relevant. Unfortunately, energy conservation depends on "remembering" the initial condition. The boundary conditions enhance the difficulty. If the

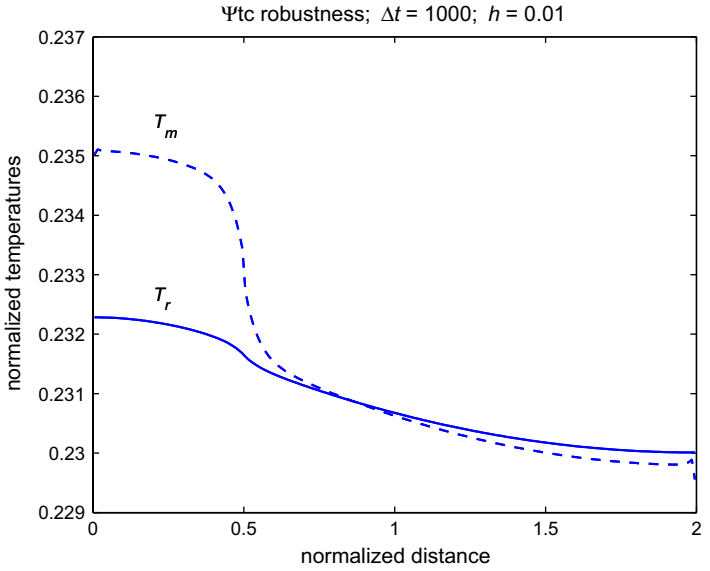

Fig. 5. Ψtc robustness test; solution after one time advance; $h = 0.01$, $\Delta t = 1000$.

initial condition is indeed "forgotten," the solution is not unique. Any equilibrium temperature $T_e = T = T_r$ is a steady-state.

For runs without Ψtc, we impose $\sigma = 1$ and determine for which magnitude Δt the iterations fail to converge. Runs using Ψtc proceed as follows. We first compute the three different σ required to have (1) a non-negative RS, (2) diagonal dominance, and (3) convergence of inner iterations. That is, the σ must satisfy the lemmas of Sections 3.1, 3.2, 3.3. The iterations commence using the largest σ. The parameter σ is fixed for each outer iteration. Experience has shown that the lemmas give an overly large σ. Hence, we use the lemmas to set σ for only the first outer iteration. Subsequent outer iterations decrease σ as follows. Recall $\sigma = 1 + \tau$ and that only when $\tau = 0$ do we solve the correct discretization of the equations. Successive outer iterations multiply τ by a constant factor, i.e., $\tau \to \alpha_\tau \tau$. The factor may be changed by the user. For small α_τ, τ decreases quickly, but the resulting linear system is harder to solve. For the hardest test, where $\Delta t = 1000$ (see below), we experimented and found better results with $\alpha_\tau = 0.5$ than with $\alpha_\tau = 0.25$.

Our tests begin with $\Delta t = 20$, a magnitude at which both modes, with and without Ψtc, converge and give nearly identical results. For this moderately large Δt, Ψtc brings the benefit of faster convergence: 37 vs. 50 CPU sec, i.e., nearly 33% faster. For $\Delta t = 100$, the two modes still converge and give very similar results, but they are now at the limit of convergence. The Ψtc run is significantly faster: 56 vs. 205 sec, an almost four-fold improvement. For $\Delta t = 200$, the non-Ψtc run does not converge. However, its final iterate temperatures still look physical; T_r is 0.5% uniformly higher than the corresponding converged Ψtc profile. Our Ψtc implementation has its own limit. The Fig. 5 result, where $\Delta t = 1000$, also fails to converge. Nonetheless, the result is physical and conserves energy to nearly 11 decimal digits. Non-convergence is evidenced by small dips in the matter temperature T_m at the cells abutting the left and right boundaries. At the end points, T_m changes very slowly from one iteration to the next. The iterations effectively stall. Although the residuals continue to decrease, they have such a slow decay that the run halts when it reaches the iteration limit. The run without Ψtc and $\Delta t = 1000$ diverges due to negative internal energies. To summarize, Ψtc not only decreases the runtime but also brings an extra degree of robustness.

5.3. Expansion of a hot aluminum sphere

In our opinion, the hardest aspect of code development is integrating a module into a multiphysics code and running "real" problems. For us, this implies simulations of multiple materials, whose properties are listed in tables, using hydrodynamics, heat conduction, radiation modules, and, naturally, AMR.

For the final test we consider the following problem. An Aluminum (Al) sphere of radius 15.5 cm is suspended in air. The initial densities are $\rho = 2.68118198$ and 0.00129 g/cm^3 for Al and air, respectively. Both materials are initially at $T = 375.936$ K.[12] There is initially no radiation energy: $E_r|_{t=0} = 0$. At $t = 0$, we inject energy into the radiation field, but only into the domain containing Al. The energy is added over 0.1 ns, at which point we have loaded a yield Y (erg) into the problem. Energy is added with a Planckian spectrum. Unless stated otherwise, the simulations presented in this section use two AMR levels; $h = 2$, 4 cm, and a base grid with $h = 8$ cm.

We compare simulations in which radiation transport is modeled by a single diffusion equation for the radiation energy density (gray diffusion) to runs where the transport is modeled with multigroup diffusion (MGD). We describe results where $Y \approx 11$ kT and $Y \approx 1$ MT.[13]

The problem simulates a strong explosion in air; the parameter choice corresponds to a nuclear source. The effects are well-known: Zel'dovich and Raizer [25] Ch. IX, Brode [5]. Initially, radiation dominates the dynamics: a fast thermal wave propagates through the surrounding air. When the wave slows to sonic speeds (of the hot air), the steep pressure gradient gives rise to a strong shock. Finally, hydrodynamics dominates. Salient effects are similar to the simulation of a point explosion using hydrodynamics and nonlinear heat conduction ([20], "Non-Self-Similar-Problem" section).

Before presenting our results, we summarize them. For the lower yield, gray and MGD simulations are very similar. However, for $Y = 1$ MT, the gray and MGD simulations differ significantly and this, we feel, is a new result. Although it contradicts established theory (Brode [5]) we believe it to be correct since it is explained by examining spectra of the radiation field (see below). Furthermore, our MGD result is corroborated by the trusted computer code LASNEX [26].

Figs. 6–8 display densities, temperatures and velocities, respectively. Each figure contains three curves. Two are from gray and MGD simulations with $Y = 11$ kT. The third curve is from a simulation using gray diffusion and a yield $Y = 1$ MT. The 1 MT curves are drawn after implementing Sachs scaling, i.e., by scaling time and radii by the cube root of the yield ratio $R_Y = (Y_1/Y_2)^{1/3}$, where $Y_1 = 11$ and $Y_2 = 1000$. Hence, while the $Y = 11$ results are taken at $t = 1$ ms, the 1 MT results are at $t = 4.48$ ms and the 1 MT radii have been divided by R_Y. Fig. 6 displays $\log_{10}(\rho/\rho_0)$, where $\rho_0 = 0.00129$ g/cm^3 is the ambient air density. Although the close agreement displayed in Figs. 6–8 may not surprise, it is indeed remarkable how well the gray scaled 1 MT curves compare with the lower yield results. The similarity of the $Y = 11$ kT gray and MGD curves indicates that gray diffusion is adequate for small Y.

The results in Figs. 6–8 are characteristic of an event transitioning from a radiation dominated regime to one dominated by hydrodynamics. Figs 6 and 7 depict a strong shock at $r = 31$ m separating from a fireball of radius 26-27 m.

In order to validate our gray $Y = 1$ MT simulation, we continue the run to $t = 7$ ms and find good qualitative agreement when we compare with Brode [5]. Quantitatively, at $t = 7$ ms, we find a strong shock at $r = 164$ m, whereas Brode finds it at $r \approx 190$ m. Both simulations show a nearly tenfold density rise at the shock, while inside the fireball, $\rho \approx 5 \times 10^{-5}$ cm^3. For the central ($r = 0$) temperature we have $T = 2.04 \times 10^5$ K at $t = 7$ ms vs. $\approx 2 \times 10^5$ K for Brode. Our fireball radius is 138 m ($\approx$160 for Brode), and our shock temperature is 1.65×10^4K ($\approx 1.6 - 1.7 \times 10^4$ for Brode).

We now compare the gray and MGD results for $Y = 11$ kT yield at the earlier time, $t = 1$ μs, when the solution is dominated by radiation. At this time, since the thermal wave is supersonic, it suffices to only examine the temperatures T and T_r, where, for both gray and MGD simulations, $T_r \doteq (E_r/a)^{1/4}$ and a is the radiation constant. (Although the Al ball has ballooned to nearly 1 m, which launches a strong shock at the Al/air interface, there is little separation between the interface and the shock. Thus, beyond 1 m, the air density is nearly the same as it was initially.) Fig. 9, which displays the temperatures, shows little difference between gray and MGD. Both models display a fireball extending to $r = 8.1$–8.4 m and a central $T \approx 2.5 \times 10^6$ K; both also display the start of the shock at the Al/air interface, as evidenced by the spike at $r \approx 0.8$ m.

[12] Inputs are tailored so that our EOS returns equal pressures for both materials, approximately 1 bar.

[13] Using the conversion 4.18×10^{19} erg/kT, the actual yields are 10.9731 kT, 0.9870682 MT, 10.9665 kT, and 0.9862604 MT for the two gray and two MGD runs, respectively.

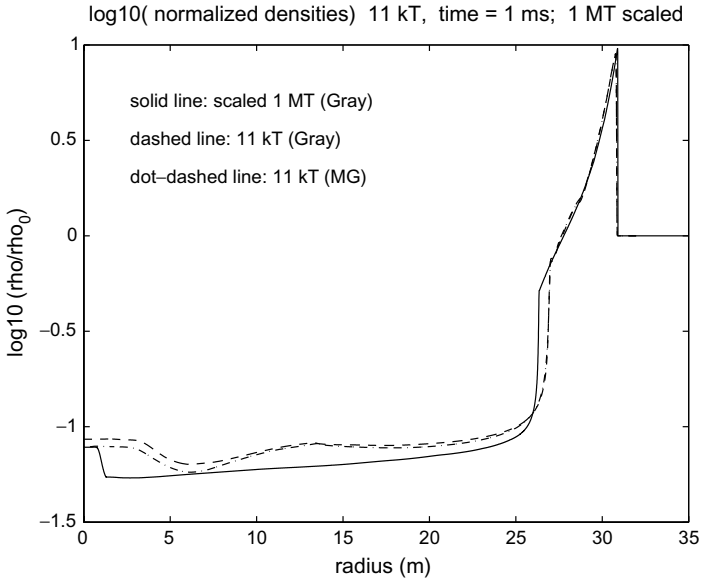

Fig. 6. Hot sphere problem. Log of normalized densities; $Y = 11$ kT yield, $t = 1$ ms, gray and multigroup diffusion; $Y = 1$ MT gray curve is scaled.

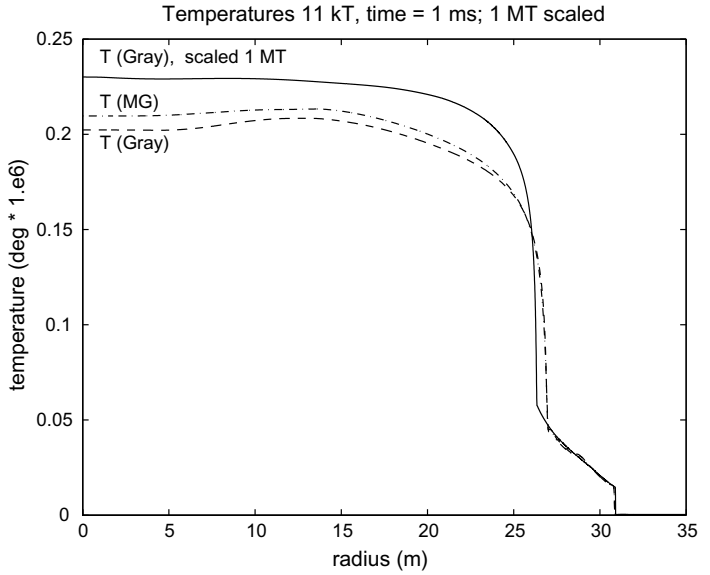

Fig. 7. Hot sphere problem. Matter temperatures T; $Y = 11$ kT yield, $t = 1$ ms, gray and multigroup diffusion; $Y = 1$ MT gray curve is scaled.

However, for high yield, the gray and MGD simulations differ dramatically. Fig. 10 displays T and T_r for $Y = 1$ MT at $t = 1$ μs.[14] We see that for gray diffusion, $T = T_r$; just as for $Y = 11$ kT. The gray diffusion thermal wave, which is still supersonic, has a front at $r \approx 30$ m. However, the MGD result is strikingly different. Multigroup diffusion lowers the central temperatures by more than 10%. More surprisingly, for MGD, T and

[14] The spatial scale of Fig. 10 cannot resolve the small, but nevertheless significant hydrodynamic effects which expand the Al sphere to $r \approx 80$ cm. For MGD, the temperature is not monotone w.r.t. to r near the origin. It falls from a central value of 2.6×10^6 deg to 1.8×10^6 at the edge of the sphere (due to the rarefying Al) then rises to 2.06×10^6 in the air.

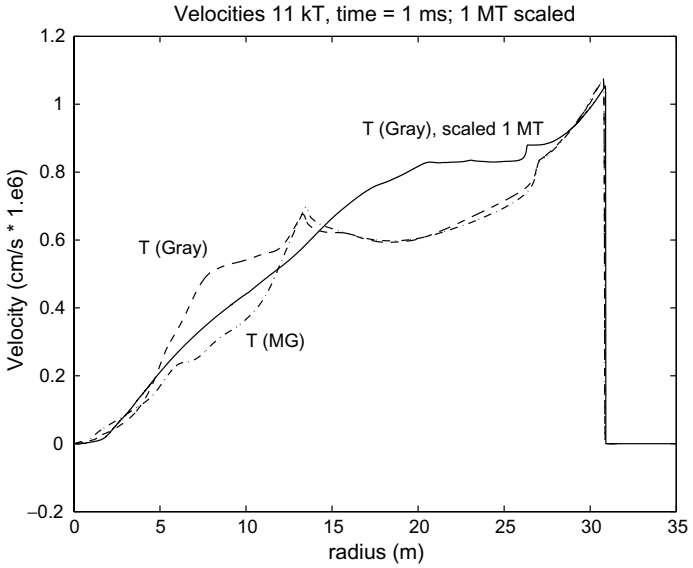

Fig. 8. Hot sphere problem. Velocities; $Y = 11$ kT yield, $t = 1$ ms, gray and multigroup diffusion; $Y = 1$ MT gray curve is scaled.

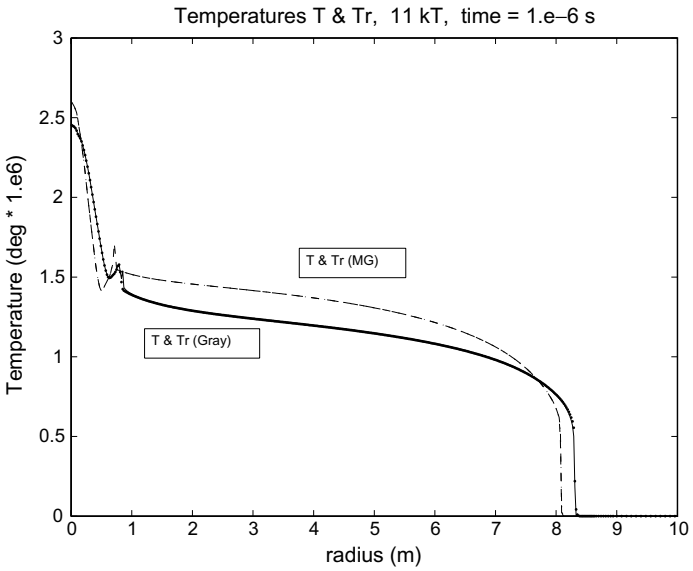

Fig. 9. Hot sphere problem. Gray and multigroup temperatures T and T_r, $Y = 11$ kT, $t = 1$ μs.

T_r are tightly coupled only out to $r \approx 20$ m. Beyond that, at $T \approx 8.5 \times 10^5$ K, T and T_r decouple. The radiation temperature extends to $r \approx 300$ m, which is the free-streaming limit.

To examine why the high yield gray and MGD simulations differ, we turn off hydrodynamics and heat conduction, repeat the simulation, and find temperatures similar to Fig. 10. This is not surprising since the dynamics are radiation-dominated. To gain more insight, we examine spectra. Fig. 11 displays the spectral radiation energy vs. frequency at 5–160 m. Evidently, the frequency-dependent air opacity is responsible. High frequency (30–200 keV) photons travel largely unimpeded whereas near the origin, the spectrum develops a hole at 10 keV. Moving away from the center, the hole progresses to lower frequencies so that at 100–200 m, the spectrum consists of two peaks, one at the high frequencies, another near the visible range. Since the latter contains little energy, the protruding radiation "tongue" of Fig. 10 is due to the high frequencies.

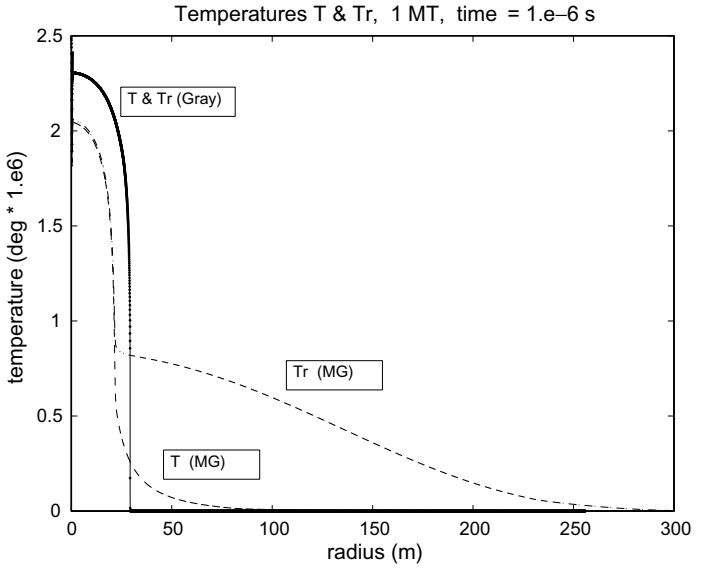

Fig. 10. Hot sphere problem. Gray and multigroup temperatures T and T_r, $Y = 1$ MT, $t = 1$ μs.

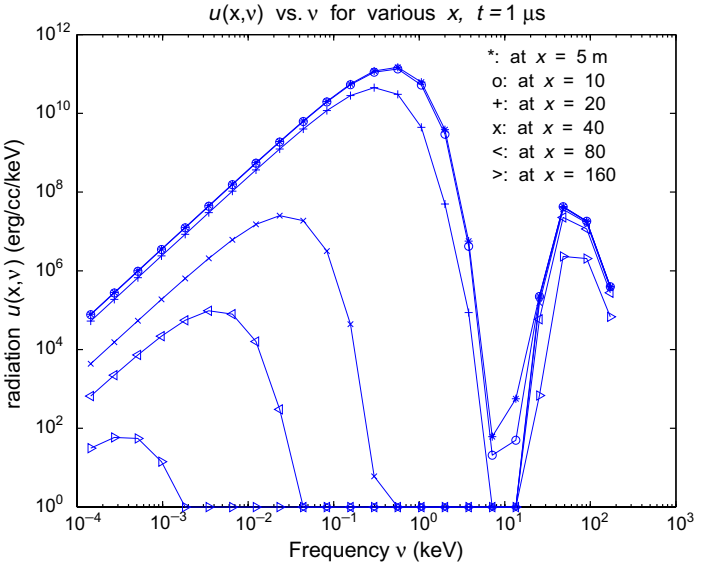

Fig. 11. Hot sphere problem. Spectral radiation energy (erg/cc/keV) vs. frequency (keV) at various radii; multigroup physics only; $Y = 1$ MT, $t = 1$ μs.

We believe that the difference between the $Y = 11$ kT and $Y = 1$ MT MGD simulations is due to the factor of 100 between the yields. Because the energy is added with a Planckian spectrum, the initial maximum temperatures differ by roughly the fourth root, or approximately 3. The initial temperatures are of order 3–5 keV and the high frequencies have a nearly Wien distribution, $\nu^3 e^{-\nu/T}$. Hence, we expect the $Y = 11$ kT spectrum to be $e^{-\nu/T}/e^{-\nu/3T}$ or $e^{-2\nu/3T}$ times smaller than the high yield case. Substituting $T = 3$ and $\nu = 100$ keV gives a very small number. The conclusion is that the $Y = 11$ kT case has an insignificant number of those energetic photons that are not absorbed by air.

We conclude the section by comparing results of the 1D spherical and 3D Cartesian versions of our code. We return to running with full functionality, i.e., with hydrodynamics, heat conduction, as well as with two

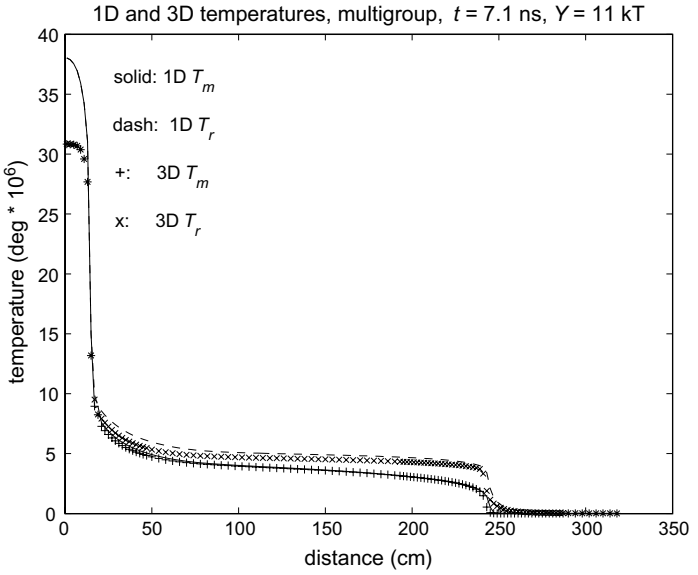

Fig. 12. Hot sphere problem. Comparison of T and T_r for Cartesian and spherical multigroup runs; $Y = 11$ kT, $t = 7.1$ ns.

AMR levels. For the Cartesian simulation, the Al "sphere" is a cube 31 cm per side (in contrast to the 1D, 31 cm diameter ball.) The difference in volumes implies that the initial central, Cartesian temperatures are necessarily smaller in order to have the same yield. Fig. 12 displays the radial 1D results and a x axis lineout of the Cartesian run. The agreement of the profiles is self-evident.

To summarize, we have simulated real-life problems, viz., air bursts with yields $Y = 11$ kT and 1 MT. We have shown that for low Y, gray and MGD give similar results. However, for large Y, they differ for early times when the dynamics are dominated by radiation. Our high yield MGD simulation contradicts results of Brode [5]. However, Brode's pioneering simulations were done many years ago when the relatively limited computational resources precluded using sophisticated modules such as MGD.

6. Conclusion/summary

We have described a numerical scheme to solve the radiation multigroup diffusion equations. The scheme is implemented in a radiation-hydrodynamic code with the patch-based AMR methodology, originally proposed by Berger and Oliger [3] for hyperbolic partial differential equations. Our scheme consists of two parts. The first, described in Sections 2 and 3, is applied on a *level* of the AMR grid layout and may be adapted to any code. This part consists of adding Ψtc to the "fully-implicit" iterative scheme of Axelrod et al. [2]. Ψtc brings an extra degree of robustness and enhances convergence of the Axelrod scheme. We have developed lemmas that determine the minimum magnitude for the Ψtc parameter τ to ensure that the iterations converge and the result is physically meaningful. The appropriate magnitude depends on the problem.

Our implementation of Ψtc is not optimal—at least for our AMR code architecture. In our code, for each AMR level, we compute a *single* scalar parameter τ. However, the levels consist of a collection of grids (rectangles in 2D) that need not be connected. If the grids are not connected, they form independent problems. Hence, it would be more efficient to use different τ for disconnected grids.

The second part of our scheme, the sync-solve (SS), addresses a specific need of our code, viz., the requirement of having an energy-conserving result on the composite grid of multiple AMR levels. For the multigroup equations, this part reduces to a coupled system of elliptic equations on the unstructured grid combining all levels. Since the SS is intended to be a small correction to the result of the level solves, we adapted the key element of the "partial temperature" scheme of Lund and Wilson [10]. This allowed reducing the multigroup SS to a collection of scalar SS's. We were then able to reuse existing software.

This paper included simulations of three problems. The first two are idealized tests of only the multigroup module. The third is a "real" problem, which uses the full capability of the code: AMR, multiple materials, etc. The first problem was chosen because of its non-triviality and the availability of analytic results with which to compare. We obtained excellent agreement and verified the convergence properties of the scheme. The second problem illustrated the benefits brought by Ψtc. We compared the conventional scheme of Axelrod et al. [2] with our Ψtc-modified version. For hard problems, Ψtc either decreased run times or ensured convergence in regimes where the conventional scheme diverged. The third problem showed that our multigroup module has been fully integrated into the code and has already extended the scientific frontier. For a high yield air burst at STP, we found that gray diffusion gives an incorrect result during the radiation-dominated regime because gray fails to capture the frequency-dependent effects of the air opacity.

Acknowledgements

We thank Dr. J. Bolstad (LLNL) for computing the revised data displayed in the Appendix and for a careful reading of the manuscript. We are grateful to Dr. M. Clover (SAIC) for many fruitful discussions. We also thank the referees for a careful and thoughtful review of our original manuscript. The paper is very much improved due to their suggestions. Unfortunately, they must remain anonymous.

Appendix A. Revised S&B table

x	T	E_r	$\epsilon(T)$	$\epsilon(E_r)$
0.0000000E+00	9.9373253E−01	5.6401674E−03	5.4E−09	5.9E−11
2.0000000E−01	9.9339523E−01	5.5646351E−03	1.8E−08	7.0E−11
4.0000000E−01	9.8969664E−01	5.1047352E−03	6.0E−09	6.2E−11
4.6000000E−01	9.8060848E−01	4.5542134E−03	9.8E−09	6.4E−11
4.7000000E−01	9.7609654E−01	4.3744933E−03	1.3E−08	6.9E−11
4.8000000E−01	9.6819424E−01	4.1294850E−03	8.2E−09	6.3E−11
4.9000000E−01	9.5044751E−01	3.7570008E−03	6.7E−09	6.3E−11
5.0000000E−01	4.9704000E−01	2.9096931E−03	7.7E−09	2.8E−11
5.1000000E−01	4.3632445E−02	2.0623647E−03	1.2E−08	6.3E−11
5.2000000E−01	2.5885608E−02	1.6898183E−03	1.3E−08	6.3E−11
5.3000000E−01	1.7983134E−02	1.4447063E−03	1.8E−08	7.0E−11
5.4000000E−01	1.3470947E−02	1.2648409E−03	1.5E−08	6.5E−11
6.0000000E−01	4.3797848E−03	7.1255738E−04	1.1E−08	6.4E−11
8.0000000E−01	6.4654865E−04	2.3412650E−04	2.3E−08	6.8E−11
1.0000000E+00	1.9181546E−04	1.0934921E−04	1.0E−08	6.1E−11

Revised S&B table [4]; time $t = 1.0$, $T_f = 0.1$. Columns 4 and 5 give maximum, absolute error estimates. Hence, at $x = 0$, entry T is correct to ±5.4E−09, i.e., has 8 trustworthy digits.

Appendix B. Diagonal dominance; large mean free paths

As noted in the footnote of Section 3.2 (and remarked by a referee), long mean free paths may lead to diffusion coefficients that overwhelm the other matrix terms. Thus, the estimate for σ, obtained in Lemma 2, may be insufficient. The matrix diagonal contains three terms of various magnitudes. The first stems from the discretization of the $\partial/\partial t$ derivative. Because we multiply by Δt, the term equals 1. The second term is due to the coupling coefficient a_g; the term equals $\Delta tc/l_g$, where $l_g = (\rho\kappa_g)^{-1}$ is the mean free path. The third term is the diffusion coefficient, which after including the time step and discretization of $\partial^2/\partial x^2$, is of the form $\Delta tcl'_g/3h^2$, where l'_g is the flux limiter-modified mean free path;

$$l'_g = 1/[(l_g)^{-1} + (3h)^{-1}(\beta + |\Delta u_g|/u_g)],$$

where β is a small, user-set constant, whose utility will become evident and $\Delta u_g/u_g$ is a normalized difference of adjoining cell-centered values.

In the limit $l_g \to \infty$, the coupling term a_g is negligible. Hence, we compare the diffusion term with unity. As $l_g \to \infty$, l'_g no longer depends on l_g. After factoring a factor of h, the diffusion term is of magnitude,

$$(\Delta tc/h)/(\beta + |\Delta u_g|/u_g).$$

The quantity β^{-1} plays the role of the maximum number of mean free paths allowed, in units of h. If the gradient of u_g is not negligible, $|\Delta u_g|/u_g$ dominates the diffusion term. If both $l_g \gg 1$ and $|\Delta u_g|/u_g \ll 1$, β dominates. In that case, we are left comparing 1 to $\Delta tc/h\beta$. The parameter β is small; we often use 10^{-4}. (However, as shown in Appendix C, 10^{-4} is too large.) Using $c = 3 \times 10^{10}$ cm/s gives a diffusion term of order

$$3 \cdot 10^{14}\Delta t/h. \tag{39}$$

If this exceeds machine precision, the σ estimate of Lemma 2 does not guarantee diagonal dominance. We are now left with problem-specific estimates. Clearly, simulations requiring small h or large Δt are problematic. Luckily, our envisioned applications yield reasonable $\Delta t/h$ ratios.

Consider two topics, ICF hohlraums and simulations of the type described in Section 5.3. For the former, mesh sizes are rarely less than 0.1 μm, i.e., $\min(h) = \mathcal{O}(10^{-5})$ cm. Luckily, in ICF, typical total simulations times are of order of tens of ns, requiring significantly smaller timesteps. Using $\max(\Delta t) = \mathcal{O}(10^{-9})$ s, makes (39) of order 10^{10}, which, when compared to unity, is six orders of magnitude above double precision.

For applications of the type presented in Section 5.3, while timesteps vary enormously, so do mesh sizes; hence, the ratio $\Delta t/h$ remains moderate. For long-time simulations requiring Δt exceeding 1 s, it is unlikely that it is necessary to resolve details less than 100 cm. Substituting these values into (39) leaves 3×10^{12}, which, is also resolved by double precision, but just barely.

Appendix C. Full physics convergence analysis

This section presents a spatial convergence analysis of the scheme as it may be used in practice. Particular attention is devoted to effects of the flux limiter and AMR. In contrast to what was analyzed at the end of Section 5.1, here we refine about a moving front.

The exactness of the solution depends upon the magnitudes of Δt and Δx. To ensure that the time step does not dominate the error, we use a very conservative value for Δt, which is much smaller than what would be used in practice. When Δt is small, Ψtc is not needed. Furthermore, we find that solutions using the FI and SI schemes are indistinguishable for our chosen Δt. We obtain the same result by solving nonlinear problems for each time step (FI) as by linearizing the equations and solving linear systems (SI). In order to save computer time, the simulations in this section use the SI scheme and do not use Ψtc.

To address concerns of a referee, we consider a stringent test and focus attention on the problem described in Section 5.3. An Al sphere of 15.5 cm radius is suspended in air. Initially, both sphere and air are at STP; the radiation field is initially zero. We load a $Y = 1$ MT source (approximately 4×10^{22} erg) into the radiation field only in the region containing Al. The source is loaded into a Planckian spectrum over a time interval $t_s = 0.1$ ns. The interval is so short that over its duration the main effects are to raise the radiation field to a high temperature and to a lesser extent also increase the matter temperature due to coupling. At $t = t_s$, most of the energy is in the radiation field inside the sphere. The radiation temperature T_r is largely uniform over the sphere and equals approximately 1.3×10^8 deg, or nearly 12 keV.

To highlight effects of the flux limiter, we examine the solution at $t = 10^{-7}$ s. In order to analyze errors due to only our multigroup scheme, we turn off all other physics, e.g., hydrodynamics. This yields profiles that are similar to those obtained with a "full physics" simulation since at $t = 10^{-7}$ s hydro effects should be negligible. (Assuming maximum sound/shock speeds of $\mathcal{O}(10^7)$ cm/s, the most that hydrodynamics can do is push the Al/air interface out a few cm while the hot sphere can radiate out to 3000 cm.)

We examine the total radiation energy density; Fig. 13 displays E_r for $r > 40$ cm. Inside the Al, E_r is much larger than what is shown in Fig. 13; it decays steeply from a central value of 2.6×10^{14} erg/cc, to 1.5×10^{12} at

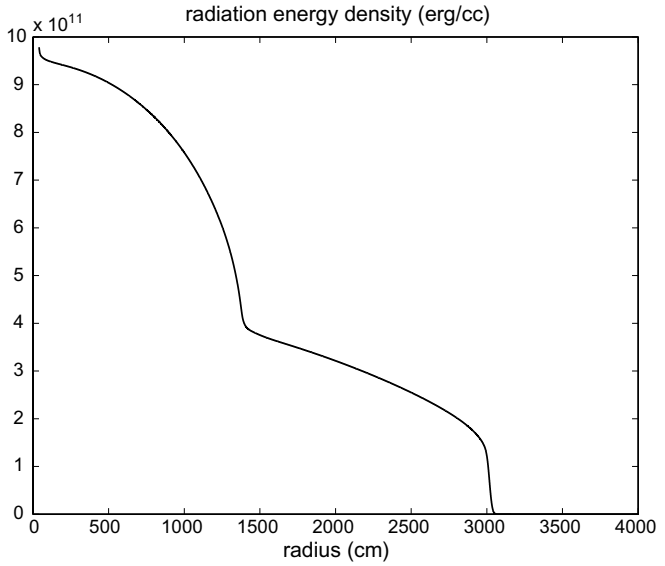

Fig. 13. Hot sphere problem. Radiation energy density E_r (erg/cc), $Y = 1$ MT, $t = 0.1$ μs, $\Delta x = 0.5$ cm. Air region.

$r = 16$, which designates the air cell adjoining the sphere. Hence, the radiation temperature decays from a central value of $T_r = 14 \times 10^6$ to 3.8×10^6 deg. The change in slope at 1400 cm is explained by examining the temperatures T_r and T; see Fig. 14. The distance $r = 1400$ marks the approximate extent of the fireball. However, radiation propagates out to $r = 3000$ cm, then drops sharply; the drop due to the flux limiter.

We identify three distinct regions in the profiles of Figs. 13 and 14. The innermost, out to $r = 1400$ denotes where we can expect the *diffusion* equations to yield an accurate representation of the physics. There, the domain is largely optically thick, as evidenced by the close agreement of T and T_r. The region $1400 < r < 2900$ denotes an optically thin region, where the diffusion approximation is expected to fail. Lastly, in the region $r > 2900$ the solution depends entirely on a *kludge:* the flux limiter. However, although at this time the limiter is dominant only near $r = 3000$, it has affected the entire solution because the propagation of the front is governed by the limiter and hence all cells out to the present position of the front have been traversed by the leading edge of the wave.

For the purposes of the convergence study, we define the results displayed in Figs. 13 and 14 as the "converged" solution. We obtain it using a uniform grid $\Delta x = 0.5$ cm and an initial $\Delta t = 10^{-16}$ s. The timestep increases by 5% each cycle but is not allowed to exceed 2×10^{-12} s. We take 50,183 steps to reach the final time. The discretization yields a light-speed Courant number $C_c \doteq c\Delta t/\Delta x = 0.12$. Although the value may seem overly cautious, it is still too large. A transport calculation would preclude any signal from propagating beyond $r = 3016$ cm. However, our finest-grid diffusion result yields $T_r = 1.8 \times 10^6$ and 12,000 deg at $r = 3016$ and 3116 cm, respectively. Although the enhanced diffusion of our result may be due to our choice of a limiter, and as analyzed by Morel [13] and Olson et al. [14] there are other limiter choices, all limiters reduce to discretizing the equation $u_t = cu_x$.

We time-lag the limiter for two reasons. (1) Flux limiting is a kludge. Thus, a time-advanced limiter is not only more complicated to implement but it does not yield a more accurate solution. (2) When a front propagates into cold material, a time-lagged limiter puts a front slightly behind where a time-advanced limiter would place it.[15] So, since the raison d'etre of a limiter is to retard the flow, we time-lag.

[15] The result may be seen by comparing two face-centered, flux limited diffusion coefficients of the form $u/|\partial_x u|$ and discretized as $(h/2)(u_0 + u_1)/|u_0 - u_1|$. Assume the front propagates into cell *0*. Let the time-lagged $u_0 = 0$ and the time advanced values be u'_0 and u'_1 with $u'_0 \ll u'_1$. After dividing by $h/2$, the time-lagged and time-advanced coefficients equal 1 and $(1 + \varepsilon)/(1 - \varepsilon)$, respectively, where $\varepsilon = u'_0/u'_1$. Thus, the time-lagged diffusion is smaller and the front does not propagate as far.

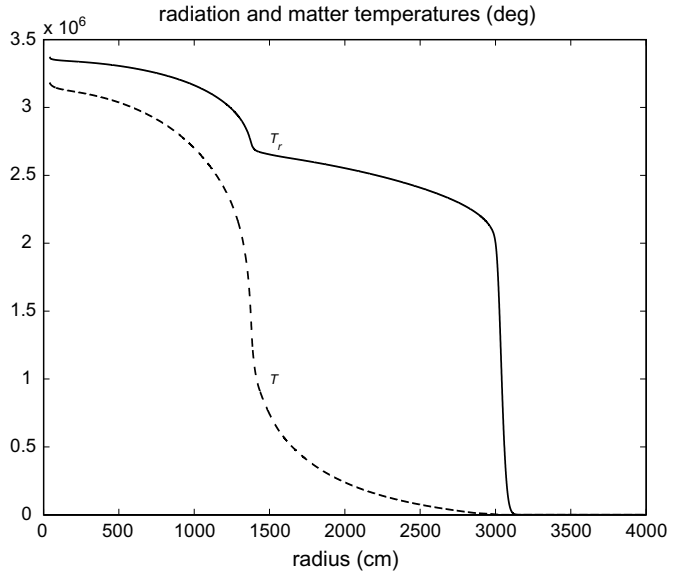

Fig. 14. Hot sphere problem. Radiation T_r and matter temperature T (deg), $Y = 1$ MT, $t = 0.1$ μs, $\Delta x = 0.5$ cm. Air region.

Before describing the convergence study, we take up two topics. The first is a truncation error analysis of a diffusion equation with a time-lagged flux limiter. If the limiter is dominant, the face-centered diffusion coefficient is $D_{i+1/2} = [(u_{i+1} + u_i)/2]/[|u_{i+1} - u_i|/\Delta x]$, where i denotes the cell index. After inserting this expression into the equation discretized with backward Euler we obtain,

$$u'_i - u_i = (C_c/2)[G_{i+1/2}(u_{i+1} + u_i) - G_{i-1/2}(u_i + u_{i-1})], \tag{40}$$

where $G_{i+1/2} = (u'_{i+1} - u'_i)/|u_{i+1} - u_i|$ and primes denote the time-advanced variable. We ignore the absolute value operator since it only serves to enforce flow down the gradient. Since G is of the form $f(t + \Delta t)/f(t)$, $G_{i\pm1/2} = 1 + \Delta t\ F$, where F has units of inverse time and its leading term is $f'(t)/f(t)$. Expanding the LS of (40) about the time-retarded value yields, $\Delta t \partial_t u + \mathcal{O}(\Delta t)^2$, while inserting the expansions of $G_{i\pm1/2}$ reduces the RS of (40) to

$$(C_c/2)[(u_{i+1} - u_{i-1}) + \Delta t U_t].$$

The term U_t is of the form $(\partial_t f/f)\Delta x \partial_x u$ and has units of u/t. The difference $(u_{i+1} - u_{i-1})$ yields $2\Delta x \partial_x u + \mathcal{O}(\Delta x^3)$. After simplifying, we obtain the truncation error of (40),

$$\partial_t u + \mathcal{O}(\Delta t) = c\partial_x u + \mathcal{O}(\Delta x^2) + C_c U_t/2.$$

The C_c term is important. It shows that even when both Δt and Δx are small, the discretization has an additional error proportional to the light-speed Courant number.

The second topic is related to the parameter β introduced at the end of Section 2. Appendix B shows that for large mean free paths the diffusion coefficient may depend solely on the sum $\beta/\Delta x + |\nabla u|/u$. Consider Fig. 13 and the domain $1500 < r < 2500$. From values at $r = 1500$, 2000, 3000, we estimate the average of $|\nabla E_r|/E_r$ to be 3.7×10^{-4}. Thus, if a particular β is deemed sufficiently small for some coarse mesh width, as the mesh is refined, the ratio $\beta/\Delta x$ may overwhelm the flux limiter. The statement has implications for both a conventional uniform-grid convergence study as well as one with AMR, since we use the same β on all levels. Unless stated otherwise, for all runs discussed in this section $\beta/\Delta x = 10^{-6}$.

We now describe the single-level convergence study. We make five runs with successively finer grids, $\Delta x = 8$, 4, 2, 1, and for the "converged" result, $\Delta x = 0.5$ cm. All runs have the same initial Δt time history. However, $\max(\Delta t)$ depends on the size of Δx in order to maintain $\max(C_c)$ at 0.12. Hence, $\max(\Delta t)$ varies from 3.2×10^{-11} to 2×10^{-12} between the coarsest and finest runs.

Our code computes cell-averaged quantities, e.g., E_r (erg/cc). On the coarsest grid, we obtain 500 values on cells centered at $4, 12, 20, \ldots$, cm. In order to have an equitable comparison, for each run, we also determine 500 average values by post-processing. In order to conserve energy, we use volume averaging.

The error is computed as follows. Let $E_{i,\Delta x}$ denote the averaged energy density in the ith coarse cell for a run with mesh size Δx. By defining the relative error,

$$e_{\Delta x} = \left[\sum_{i=1}^{500}\left(E_{i,\Delta x} - E_{i,0.5}\right)^2\right]^{1/2} \Bigg/ \left[\sum_{i=1}^{500}\left(E_{i,0.5}\right)^2\right]^{1/2}, \tag{41}$$

we obtain

$$[e_8, e_4, e_2, e_1] = [0.4820, 0.2436, 0.06969, 0.03475].$$

The ratio of successive errors,

$$[(e_8/e_4), (e_4/e_2), (e_2/e_1)] = [1.98, 3.50, 2.01].$$

Since the ratios are approximately two, our results suggest first (rather than second) order convergence.

Lastly, we compare results of a run using AMR with an "equivalent" run that uses a uniform grid. For the AMR run, we use a base L0 grid with $\Delta x = 8$ cm. We use two refinement levels, each refines by a factor of two. The run begins with $\Delta t = 10^{-16}$, and we increase Δt as before until reaching $\max(\Delta t) = 3.2 \times 10^{-11}$. Because we refine in both space and time, $C_c = 0.12$ on all levels. The parameter $\beta = 8 \times 10^{-6}$; hence, $\beta/\Delta x$ varies from 10^{-6} to 4×10^{-6} between the coarsest and finest levels. The refined levels adapt to the Al/air interface (at $r = 15.5$ cm) and around the position of $\max[|\nabla(E_r)|/E_r]$. At the end of the run, the grid layout is: $0 < x < 96$ and $2944 < x < 3392$ for the L1 level ($\Delta x = 4$) while: $0 < x < 48$ and $2976 < x < 3360$ for L2 ($\Delta x = 2$). We compare errors of the AMR run as above, by forming cell averages of the 500 cells centered at $4, 12, 20, \ldots$, cm. The error on the AMR run is

$$e_{\mathrm{AMR}} = 0.06963.$$

Since for the AMR run, the finest level $\Delta x = 2$ cm, we compare e_{AMR} with the error of a uniform-grid run where $\Delta x = 2$ cm, i.e., with $e_2 = 0.06969$. To three significant digits, the errors are essentially equal. The uniform-grid run uses 2000 cells, while at the end of the simulation, the AMR run has 676 cells.

To summarize, we find that when the solution depends on the flux limiter, spatial convergence reduces to first, instead of second order. The effect reminds us of what happens to hydrodynamic schemes in the presence of shocks: in smooth parts of the flow, the solution may be second order convergent, but in regions traversed by shocks, the scheme reverts to first order. In closing, we note an additional source of error, which we did not quantify. The simulations of this section use real materials whose properties (internal energies, opacities, etc.) are given by tables. Table lookups have errors that depend on the schemes used to interpolate between table data.

References

[1] A.S. Almgren, J.B. Bell, P. Colella, L.H. Howell, M. Welcome, A conservative adaptive projection method for variable density Incompressible Navier–Stokes equations, J. Comp. Phys. 142 (1988) 1–46.

[2] T.S. Axelrod, P.F. Dubois, C.E. Rhoades Jr., An implicit scheme for calculating time- and frequency-dependent flux limited radiation diffusion in one dimension, J. Comp. Phys. 54 (2) (1984) 205–220.

[3] M.J. Berger, J. Oliger, Adaptive mesh refinement for hyperbolic partial differential equations, J. Comp. Phys. 53 (1984) 484.

[4] J.H. Bolstad, private communication, Lawrence Livermore National Laboratory, 2006.

[5] H.L. Brode, Review of nuclear weapon effects, Ann. Rev. Nucl. Sci. 18 (1968).

[6] O.H. Hald, A.I. Shestakov, Stability of stationary solutions of the multifrequency radiation diffusion equations, SIAM J. Appl. Math. 65 (1) (2004) 175–193.

[7] L.H. Howell, J.A. Greenough, Radiation diffusion for multi-fluid Eulerian hydrodynamics with adaptive mesh refinement, J. Comp. Phys. 184 (2003) 53–78.

[8] C.T. Kelley, D.E. Keyes, Convergenge analysis of pseudo-transient continuation, SIAM J. Numer. Anal. 35 (1998) 508.

[9] C.D. Levermore, G.C. Pomraning, A flux-limited diffusion theory, Astrophys. J. 248 (1981) 321–334.

[10] C.M. Lund, J.R. Wilson, Some numerical methods for time-dependent multifrequency radiation transport calculations, Lawrence Livermore Natl. Lab. report UCRL-84678, July 29, 1980.

[11] D. Mihalas, B. Weibel-Mihalas, Foundations of Radiation Hydrodynamics, Dover Publications, Inc., Mineola, New York, 1999, ISBN 0-486-40925-2.
[12] J.E. Morel, E.W. Larsen, M.K. Matzen, A synthetic acceleration scheme for radiative diffusion calculations, J. Quant. Spectrosc. Radiat. Transfer 34 (3) (1985) 243–261.
[13] J.E. Morel, Diffusion-limit asymptotics of the transport equation, the $P_{1/3}$ equations, and two flux-limited diffusion theories, J. Quant. Spectrosc. Radiat. Transfer 65 (5) (2000) 769–778.
[14] G.L. Olson, L.H. Auer, M.L. Hall, Diffusion, P_1, and other approximate forms of radiation transport, J. Quant. Spectrosc. Radiat. Transfer 64 (2000) 619–634.
[15] G.J. Pert, Physical constraints in numerical calculations of diffusion, J. Comp. Phys. 42 (1981) 20–52.
[16] G.C. Pomraning, The Equations of Radiation Hydrodynamics, Dover Publications, Inc., Mineola, New York, 2005, ISBN 0-486-44599-2.
[17] J.N. Shahid, R.S. Tuminaro, H.F. Walker, An inexact Newton method for fully coupled solution of the Navier–Stokes equations with heat and mass transport, J. Comp. Phys. 137 (1997) 155–185.
[18] A.I. Shestakov, J.A. Harte, D.S. Kershaw, Solution of the diffusion equation by finite elements in lagrangian hydrodynamic codes, J. Comp. Phys. 76 (2) (1988).
[19] A.I. Shestakov, L.H. Howell, J.A. Greenough, Solving the radiation diffusion and energy balance equations using pseudo-transient continuation, J. Quant. Spectrosc. Radiat. Transfer 90 (2005) 1–28.
[20] A.I. Shestakov, Time-dependent simulations of point explosions with heat conduction, Phys. Fluids 11 (5) (1999).
[21] A.I. Shestakov, J.H. Bolstad, An exact solution for the linearized multifrequency radiation diffusion equation, J. Quant. Spectrosc. Radiat. Transfer 91 (2) (2005) 133–153.
[22] B. Su, G.L. Olson, Non-grey benchmark results for two temperature non-equilibrium radiative transfer, J. Quant. Spec. Radiat. Trans. 62 (1999) 279–302.
[23] B. Su, G.L. Olson, An analytical benchmark for non-equilibrium radiative transfer in an isotropically scattering medium, Ann. Nucl. Energy 24 (13) (1997) 1035–1055.
[24] R.S. Varga, Matrix Iterative Analysis, Prentice-Hall, Inc., Englewood Cliffs, New Jersey, 1962.
[25] Ya.B. Zel'dovich, Yu.P. Raizer, Physics of Shock Waves and High-Temperature Hydrodynamic Phenomena, Dover, 2001, 0-486-42002-7.
[26] G.B. Zimmerman, W.L. Kruer, Comments in Plasma Physics and Controlled Fusion 2 (51) (1975).
[27] G.B. Zimmerman, private communication, Lawrence Livermore National Laboratory, 2005.